Influence of Spray Angle on Microstructure and Lifetime of Suspension Plasma-Sprayed Thermal Barrier Coatings

Wellington Uczak de Goes[1] · Mattias Ossiansson[1] · Nicolaie Markocsan[1] · Mohit Gupta[1] · Petra Honnerová[2] · Zdeněk Veselý[2]

Abstract Thermal barrier coatings (TBCs) are widely utilized in gas turbine engines for power generation. In recent years, the application of TBCs in automotive has been introduced to improve engine efficiency. Low thermal conductivity and high durability are desired coating properties for both gas turbine engines and automotive. Also, suspension plasma spraying (SPS) permits a columnar microstructure that combines both properties. However, it can be challenging to deposit a uniform columnar microstructure on a complex geometry, such as a gas turbine component or piston head, and achieve similar coating characteristics on all surfaces. This work's objective was to investigate the influence of spray angle on the microstructure and lifetime of TBCs produced by SPS. For this purpose, SPS TBCs were deposited on specimens using different spray angles. The microstructures of the coatings were analyzed by image analysis for thickness, porosity, and column density. Thermal and optical properties were evaluated on each TBC. Lifetime tests, specifically designed for the two applications, were performed on all investigated TBCs. The lifetime results were analyzed with respect to the TBC microstructure and thermal and optical properties. This investigation showed that there is a limit to the spray angle that achieves the best compromise between TBC microstructure, thermal properties, optical properties, and lifetime.

Keywords complex geometry substrate · suspension plasma spraying · thermal barrier coatings

✉ Wellington Uczak de Goes
  welucz@hv.se; wellingtongoes@gmail.com

[1] University West, Trollhättan, Sweden

[2] University of West Bohemia, Pilsen, Czech Republic

Introduction

Energy requirements are increasing worldwide, while at the same time, concern regarding pollution is an all-time high. Recent forecasts predict that by 2030, two billion motor vehicles will be on the roads (Ref 1). In this context, even a tiny fraction of increased engine efficiency can make huge differences in emissions and fuel consumption. Similar demands are reported in the gas turbine industry, where efficient and environmentally friendly engines are the highest priority (Ref 2, 3). Despite the fact that these are different applications with specific requirements, thermal barrier coatings (TBCs) are a promising technical solution, as they have already demonstrated their capability to enhance the efficiency of engines used in both automotive and energy applications (Ref 4-10).

Thermal barrier coatings (TBCs) are multilayered coating systems used to protect the hotter parts of an engine against high temperature, wear, oxidation, and corrosion (Ref 11, 12). The first layer of a TBC is the bond coat. The bond coat is sprayed on the substrate and has specific functions. The bond coat prevents the substrate from undergoing corrosion and oxidation during high-temperature exposure. Another function of the bond coat is to improve the adhesion of the top coat (Ref 13). The TBC's second layer is the top coat, which is sprayed over the bond coat. The top coat primarily provides thermal protection to the substrate. The top coat material needs to possess thermal properties such as low thermal conductivity, low specific heat, a high melting point, and phase stability (Ref 14). Top coats should also have specific properties, such as high thermal cycling life, erosion resistance, and proper adherence to the bond coat (Ref 13, 15).

TBCs cover a broad spectrum of products; hence, numerous spraying techniques aim to compromise between

the process and the coating microstructure, i.e., atmospheric plasma spray (APS), high-velocity oxy fuel (HVOF), physical vapor deposition (PVD), and chemical vapor deposition (CVD). In this work, bond coat spraying was produced by high-velocity air fuel (HVAF) spray, and the top coats were deposited by suspension plasma spray (SPS). HVAF is a thermal spray process designed to produce dense metallic coatings with high bonding strength. In this process, air and fuel gas are injected into the combustion chamber, where an electric spark plug ignites the mixture (Ref 16, 17). This mixture is then expelled through a nozzle, accelerating the feedstock particles to velocities of 1200 m/s. A low flame temperature combined with a high velocity results in dense coatings with minimal formations of pores and oxides (Ref 16). In contrast, SPS is a thermal spray technique designed to generate finely structured ceramic coatings. In this process, submicron or nanosized powders (solute) are dispersed in a solvent, e.g., water or alcohol (or a mixture). This liquid feedstock (suspension) is injected into a plasma plume, where it undergoes atomization to form fine droplets. The solvent evaporates due to the high temperatures, while the particles, partially or fully molten, agglomerate. The impinging particles are deposited on the bond coat and build up the top coat in layers (Ref 18, 19).

In SPS, the coating buildup is controlled by different factors. The momentum and interaction of the particle with the plasma plume are the most notable. Small droplets have low momentum because of their low weight. Small droplets lead to coatings deposited at shallow angles on the surface peaks, causing a shadowing effect. Large particles with higher momentum due to higher weight have a straight trajectory, which impacts the substrate perpendicularly and forms a typical lamellar coating (Ref 20). Few works have investigated the correlation between the complex geometry of real parts and coating properties sprayed on buttons. Bernard et al. (Ref 21) applied an SPS coating on a turbine blade. As a result, coating microstructural differences and thickness discrepancies were observed along the different areas of the blade. Caio and Moreau (Ref 22) also investigated SPS coating deposition on complex shapes, showing that the coating deposited is directly proportional to the radius of curvature. For example, the amount of coating material deposited decreases as the radius of curvature decreases. This condition could be associated with piston applications. In previous work (Ref 23), the authors investigated different microstructures produced on automotive pistons and the physical properties of the coatings. However, a systematic study with defined spray angles and coating property evaluation has yet to be performed.

This paper's objective is to explore the influence of different spray angles on the microstructure, properties, and lifetime of SPS TBCs designed for automotive and energy applications. Different deposition conditions were used for a selected TBC system on coupon specimens under various spray angles. The microstructure and porosity, thermal, and optical properties were characterized. Also, the lifetime was evaluated by flame rig testing, thermal cyclic fatigue (TCF), and erosion testing. A tradeoff was investigated between the spray angles of the complex geometry part and the TBC microstructural properties, which leads to a limitation on the spray angle.

Materials and Methods

Experimental Setup

Two sets of samples were produced and investigated, one for energy applications and one for automotive applications, to cover the requirements for both applications. The substrate used for the automotive application study was a commercial medium carbon vanadium microalloyed steel (38MnSiVS5) in the form of buttons (25.4 mm diameter x 6 mm thickness). For the energy application, HASTELLOY® X buttons with the same dimensions as for automotive were used, commercially acquired from Siemens Energy AG, Sweden. For the thermal diffusivity measurement using laser flash analysis, HASTELLOY® X plates with dimensions of 25 x 25 x 1.54 mm were sprayed.

The thermal spray experimental setup (Fig. 1 and Table 1) was as follows: Four sets of TBCs with the HVAF bond coat sprayed perpendicularly on the substrate and the top coats under various angles. One set of TBCs with the bond coat sprayed under a different angle with the top coat sprayed perpendicularly to the surface. The reason for selecting only one variant of spray angle for HVAF spraying was that, based on experience, HVAF spraying is not expected to be very sensitive to minor variations in spray angle.

Bond Coat Deposition

The bond coat was sprayed with an M3 supersonic spray gun (Uniquecoat Technologies LLC, USA) using a 250-mm-long de Laval nozzle designated 4L4C with an exit diameter of 22.5 mm. Before bond coat deposition, the buttons were cleaned with ethanol and then mounted on a rotating fixture fastened to a turntable. The buttons were then hot-grit-blasted using Al_2O_3 particles with 180 mesh grit to a surface roughness of Ra 3 $\approx$ μm according to the parameters in Table 2. The samples were then preheated to approximately 150 °C; then, the bond coat was deposited. The feedstock selected was a commercial, gas atomized MCrAlY (AMDRY 386, Oerlikon Metco, Switzerland), which is a metallic powder suitable for automotive and
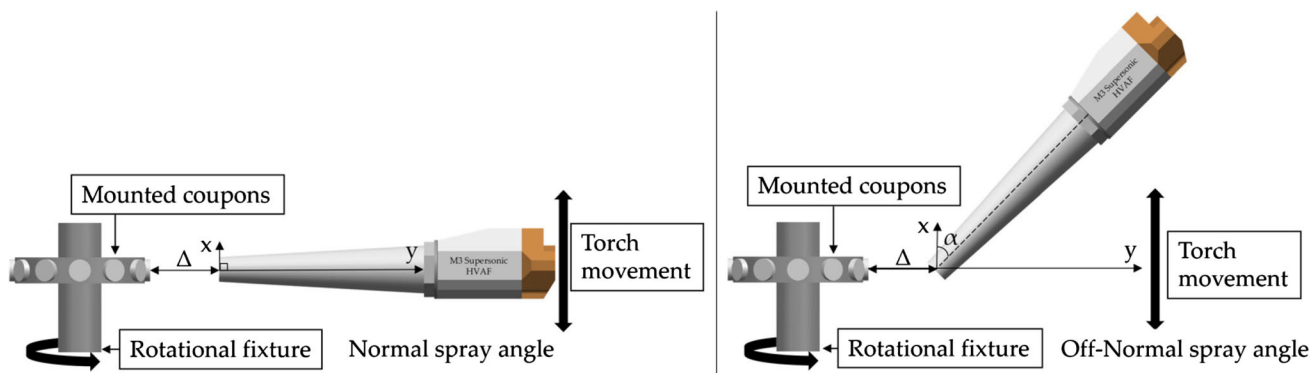
Fig. 1 Illustrating the change in spray angle between the normal and off-normal spray gun position where α is the change in spray angle to the substrate plane, and Δ is the spray distance from the spray gun's center axis. The black vertical arrows indicate the torch movement. The figure is merely a representation of M3 supersonic spray gun, but it applies to the Axial III spray gun and is not done in scale

Table 1 The experimental setup for the TBC deposition showing different spray angles. "T" stands for top coat and "B" for bond coat where the followed numbering is the angle in degrees

	Top coat	Bond coat
Sample nomenclature	Spray angle [deg]	Spray angle [deg]
T90	90	90
T30	30	90
T50	50	90
T70	70	90
T90B45	90	45

Table 2 Hot-grit blasting HVAF parameters

Air pressure [MPa]	Fuel 1 pressure [MPa]	Fuel 2 pressure [MPa]	Carrier gas [L/min]	Feed [%]	SoD [mm]	Surface speed [m/min]	Step [mm/rev]	Strokes
0.83	0.69	0.55	60	20	350	100	5	2

energy applications. The feedstock material composition was Ni22Co17Cr12Al0.5Hf0.5Y0.4Si [wt.%] with a particle size range of -63 + μm and had a spherical morphology.

The HVAF bond coat process was used at a spray angle of 45° between the spray axis and substrate plane for one set of samples and 90° for the rest of the sets, as introduced in Sect. "Experimental Setup". The standoff distance was set to 350 mm as measured perpendicularly from the nozzle exit to the substrate plane. The target thickness for the bond coat was 200 μm, and the spray parameters are shown in Table 3.

Top Coat Deposition

The SPS top coats were sprayed with an Axial III spray gun (Northwest Mettech Corp., Canada) and spray parameters according to Table 4. The feedstock was commercial yttria-stabilized zirconia (8YSZ) suspended in ethanol with a solid load of 25 wt.% and particle size d_{50} of approximately 0.5 μm (Treibacher Industrie AG, Austria). The solid YSZ particles were fused and crushed with irregular morphology. The substrate was preheated using two heat strokes with a plasma gun. The target thickness for the top coat was 300 μm.

Coating Characterization

Surface Topography

The topography of the coatings was evaluated using a Hitachi TM3000 tabletop SEM (Hitachi Ltd, Japan). Furthermore, the surface roughness was measured using a Profilm 3D profilometer with white light interferometry (WLI) (Filmetrics Inc., USA). A total of 10 measurements per sample were taken at different, evenly spaced locations.

Table 3 Spray parameters for deposition of HVAF bond coat

Air pressure [MPa]	Fuel 1 pressure [MPa]	Fuel 2 pressure [MPa]	Carrier gas [L/min]	Feed [g/min]	SoD [mm]	Surface speed [m/min]	Step [mm/rev]	Strokes [90°/45°]
0.77	0.69	0.72	60	150	350	100	5	9/31

Table 4 Parameter setup for the deposition of SPS top coat

Current [A]	Total gas flow [L/min]	Power [kW]	Enthalpy [kJ]	Ar/N_2/H_2 [%]	Atomizing gas [L/min]	Slurry feed [mL/min]	Substrate temp. [°C]	Step [mm/rev]	Strokes [90°/70°/50°/30°]
200	300	124	12.5	43/28/28	20	105	130	3.5	45/45/50/85

The data were postprocessed with Filmetrics software using a 5 x 5 Gaussian spatial filter.

Metallographic Preparation

The samples were cold mounted in a vacuum in a two-part process, first using a low viscosity epoxy (Logitech 2-part Epoxy Pack 301, Logitech Materials Technologists & Engineers, UK). With this procedure, all the open porosity would be filled with resin, preventing microstructural changes or damage during the cutting process. In the next step, the mounted samples were cut utilizing a Struers Secotom 10 with an abrasive cutting disk. The sectioned samples were cold mounted again using Buehler EpoThin 2 Epoxy for easy handling. The sample preparation for the coatings was completed with successive grinding and polishing steps using the Buehler Power Pro 5000 (Buehler Ltd, USA) until achieving a final roughness of Ra $\approx$ 0.05 μm.

Microstructure Analysis

After the samples were prepared for microstructural analysis, cross-sectional micrographs were taken using a tabletop SEM. To obtain accurate micrographs, the entire cross section was evaluated so that the selected micrographs are representative of the entire coating.

The thickness of both the bond coat and the top coat was further measured using the method described in Ref 24. Several micrographs were taken at 200x spread along the cross section and analyzed with image analysis software (ImageJ). The number of measurements for the top coat thickness was 200, due to height variations, and there were 75 measurements for the bond coat.

The columnar density was measured using the same tools described for the thickness measurement (Fig. 2) and based on the method described in Ref 24. The calculation was performed by drawing a horizontal line at the center of the coating micrograph, and then manually assessing the number of interstitial gaps that cross that line, subtracting one, and then dividing that number by the length of that line. Five micrographs per sample at 250x were used, and five measurements per micrograph were taken.

Porosity Measurement

The porosity measurement utilized a two-magnification image analysis procedure as presented in Ref 25. The coarse porosity, including pores with an area >2 μm², was assessed with 500x magnification. While the fine porosity, including pores with an area <2 μm², was assessed with 5,000x magnification. To ensure the reliability of the results, each layer was evaluated fifteen times along the low and high magnifications at the cross section. The total porosity was the sum of the fine and coarse porosities.

Thermal Properties

Laser flash analysis (LFA) was used to assess the thermal properties of the coatings with the equipment Netzsch LFA 427 (Netzsch, Selb, Germany). Due to the sample holder size, the first step was to decrease the sample size to round buttons of 10 mm in diameter using water jet cutting. After the samples were cut, both sides were covered with a thin layer of graphite to improve the absorption and emission properties. The sectioned samples were subsequently positioned in the equipment, where a laser pulse heated the backside of the samples. The pulse produced a heat flux within the sample that was sensed on the sample surface with an infrared (IR) detector. Based on the IR detector data, the thermal diffusivity was established (Ref 26).

The thermal conductivity is determined with Eq. 1 based on the thermal diffusivity results.

$$\lambda = \alpha * Cp * \rho \qquad (Eq\ 1)$$

where λ is the thermal conductivity (W/(mK)), α is the thermal diffusivity (m²/s), Cp is the specific heat capacity

Fig. 2 An example of the measurement of the columnar spacing of sample T90.

300 um
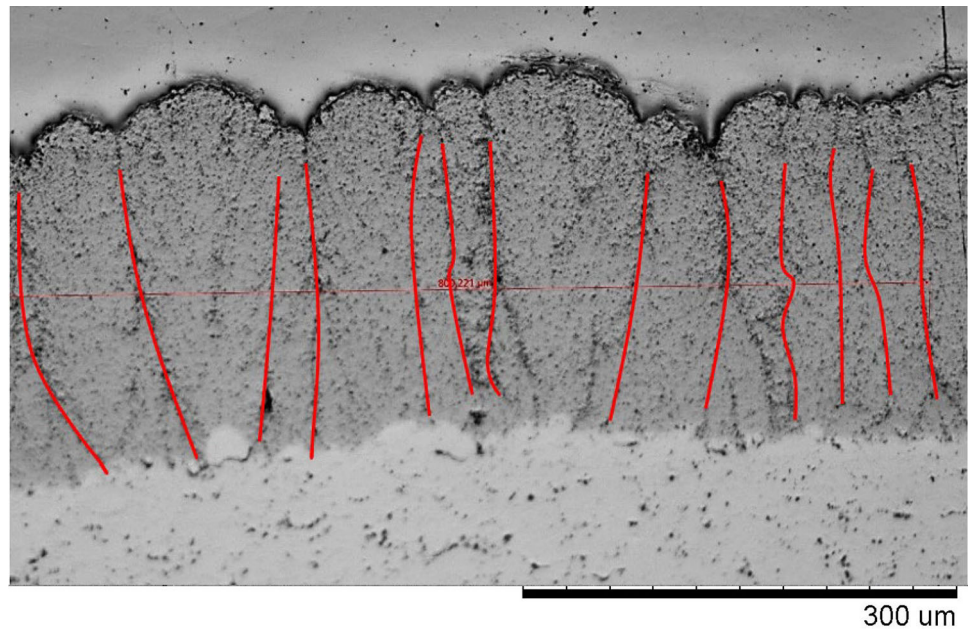
(J/(gK)) used from previous measurements reported in Ref 26, and ρ is the coating density (g/m^3) assessed from Eq. 2.

$$\rho = \left(\frac{100 - \text{total porosity}(\%)}{100}\right) * \text{(density of the fully dense coating)} \quad \text{(Eq 2)}$$

The coating density was determined based on the fully dense YSZ value from the literature (6.1 g/cm^3) (Ref 26) and the coating porosity.

Optical Properties

The emissivity, adopted as the base for the radiation heat transfer, was the optical property selected for this study. The emissivity of the surface determines the efficacy of the surface to emit radiation (Ref 27, 28). The samples utilized in this measurement were limited to the HASTELLOY® X substrate and were measured together with the same bond coat. This is important because many ceramic materials are partially transparent to thermal radiation, implying that if this coating was standalone or if different bond coats were used, it would affect the results (Ref 29).

Before testing, the samples were polished using a Carbimet Grit 360 (Buehler Ltd, USA) to avoid differences in surface profile (roughness) that could influence the results; in an actual application in real engines, the coatings should be polished. Different methods were utilized for the different temperatures. For room temperature measurement, the SNHRRT (spectral normal hemispherical reflectivity at room temperature) method was used (Ref 28). While for higher temperatures, the SNEHT (spectral normal emissivity at high temperature) method was used (Ref 30).

The SNHRRT apparatus consists of a Fourier transform infrared (FTIR) spectrometer, an integrating sphere accessory, and a calibrated reflectivity standard (Ref 28). This measurement method is based on radiation emitted from the spectrometer reaching the sample placed on the integrating sphere. Inside the integrating sphere, the reflected radiation from the sample extends in all directions until it reaches the detector (Ref 28).

Assuming an opaque material, it is possible to evaluate the sample emissivity according to Kirchhoff's law (Ref 27); see Eq. 3.

$$R + E = 1 \quad \text{(Eq 3)}$$

where R is the sample absolute reflectivity, and E is the sample emissivity.

The emissivity uncertainty is evaluated as a combined standard uncertainty of all uncertainties with coverage Factor $k = 2$. This includes repeatability of reflectivity measurement, calibration, and homogeneity of reference reflectivity standard, inserting repeatability of integrating sphere system, and atmospheric spectral absorption. The uncertainty depends on the wavelength and measured reflectivity values.

The SNEHT method assesses the spectral normal emissivity independent of temperature. This apparatus contains an FTIR spectrometer, a laboratory blackbody, a laser system for heating samples, and a system for the sample surface temperature measurement. For this test, both radiation sources (black body and sample) are positioned outside the spectrometer against each other. The radiation collection from both sources is provided by a rotary parabolic mirror placed in between, and the

spectrometer detects the radiation from the sources. Subsequently, the emissivity of the sample is evaluated (Ref 30).

As with the measurement method at room temperature, the emissivity at high temperature is subjected to uncertainties that are also determined as a combined standard uncertainty of all particular uncertainties with a coverage Factor of $k = 2$. Uncertainty sources are the measured sample and blackbody spectral signals, the measured sample surface and surrounding temperatures, the blackbody temperatures, the blackbody effective emissivity, and the surrounding emissivity (Ref 31).

Coating Testing

The coating performance as a TBC for automotive and energy applications underwent the various tests described in the following sections.

Flame Rig Test

To replicate similar combustion engine working conditions, assessing the high heat cycle presented during combustion and the subsequent cooling of the surfaces and as published previously by the authors (Ref 32), a flame rig test was employed in collaboration with Jönköping University, Sweden. In this apparatus, two samples were tested simultaneously with a specific timed cycle (6 s) between an oxyacetylene torch and a cooling nozzle. The coating temperature was measured using a K-type thermocouple mounted on the sample side and logged with a Keyence NR-H7 W. The temperature during heating was approximately 700 °C and approximately 600 °C during cooling. A comprehensive report of the apparatus is provided in Ref 32, 33.

Periodic checking of the torch was necessary because of soot formation on the torch tip, which affects the flame shape and, therefore, the heat distribution. The implemented failure criterion was an observed 10% spallation, and to check the reliability, two samples of each parameter were tested. After testing, the failed samples were examined with SEM in cross section and compared with previous work (Ref 32, 33).

Thermal Cyclic Fatigue (TCF) Test

For energy applications, the TCF performance of the samples was tested in an Entech ECF 14/16 HV (Entech Energiteknik AB, Sweden) furnace according to the method described in Ref 34. This method is well practiced in industry and was chosen because it replicates the heating and cooling that the coatings would experience during service (Ref 34). The sprayed buttons were placed with the coating side facing up. The samples were isothermally heated at atmospheric pressure to 1100 °C for 1 h and then rapidly cooled with compressed air to approximately 100 °C for 10 minutes. After 10 s of cooling, a top-view photo was automatically taken by a webcam to distinguish contrast differences due to coating cracks and spallation. The failure criterion adopted was 20% coating spallation; once this was achieved, the sample was carefully removed and prepared for characterization. As performed in the flame rig test, to check the consistency of the test, two samples of each parameter were tested.

Erosion Test

The erosion tests were carried out in an air-jet erosion rig, the TR-470 (DUCOM, Netherlands). The test followed the ASTM G76-13 standard (Ref 39). This rig facilitates testing at different sets of parameters; particularly for this work, the impingement angle was set at 90° for maximum kinetic impact energy to the coating. The erodent used was alumina (Al_2O_3) particles of irregular, angular morphology with an average particle size of 50 ± 10 μm. The distance between the nozzle and the sample was held at 10 mm, and the test was conducted at room temperature. The erodent was dried in an oven at 125 °C for a minimum of 24 h to avoid clogging. Before and after the test, the samples were ultrasonically cleaned from excess material and erosive debris and then weighed using a PCE AB-100 high precision scale (PCE-Instruments GmbH, Germany); five measurements were taken for each sample. Two samples of each batch were tested, and one extra T30 sample was used as a test sample for the parameter setup when testing exposure time. Table 5 shows the overall erosion parameters based on a previous study by Algenaid et al. (Ref 36); however, the exposure time was reduced to 30 s to reduce the risk of coating penetration for all samples. An additional 60 s was included in the test of the T90 sample for comparison with a previous study (Ref 36). Five evenly spaced erosion indents were performed for each sample. The erosion rate was calculated as the ratio of mass loss of

Table 5 Air-jet erosion test parameters

Erosion test parameters	Set
Air pressure (bar)	0.25
Particle velocity (m/s)	30
Flow rate (g/min)	2 ± 0.25
Erodent	Alumina
Grit size (μm)	50 ± 20
Angle (deg.)	90
Exposure time (s)	30 (and 60)
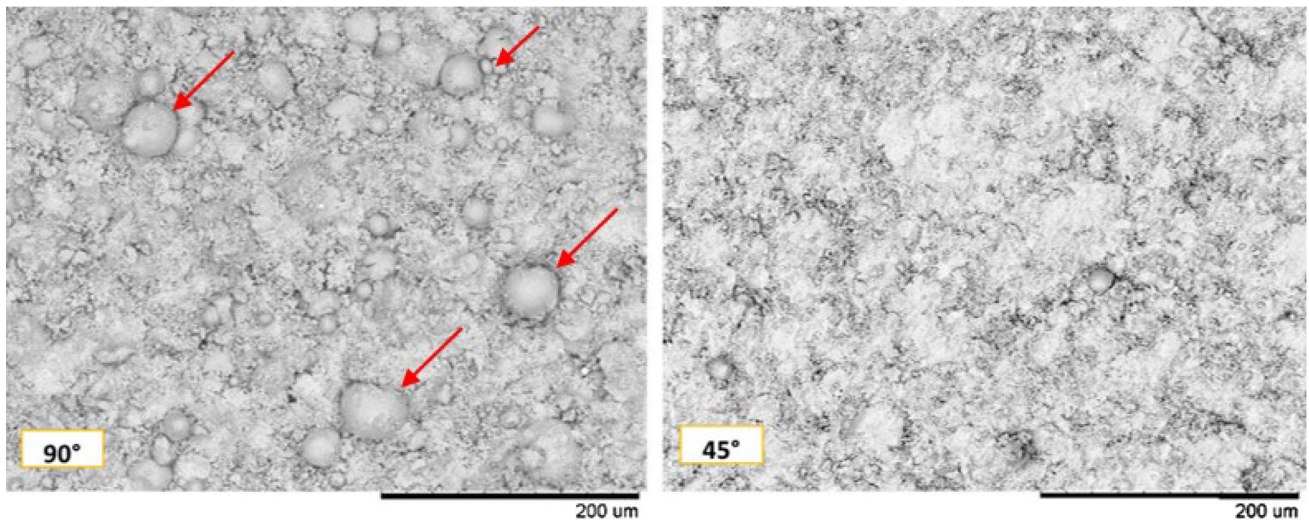
Fig. 3 (Left) micrograph of AMDRY 386-HVAF at 90° spray angle and (right) micrograph of the bond coat sprayed with HVAF at 45° spray angle. Red arrows mark the larger semi-deformed particles (Color figure online)
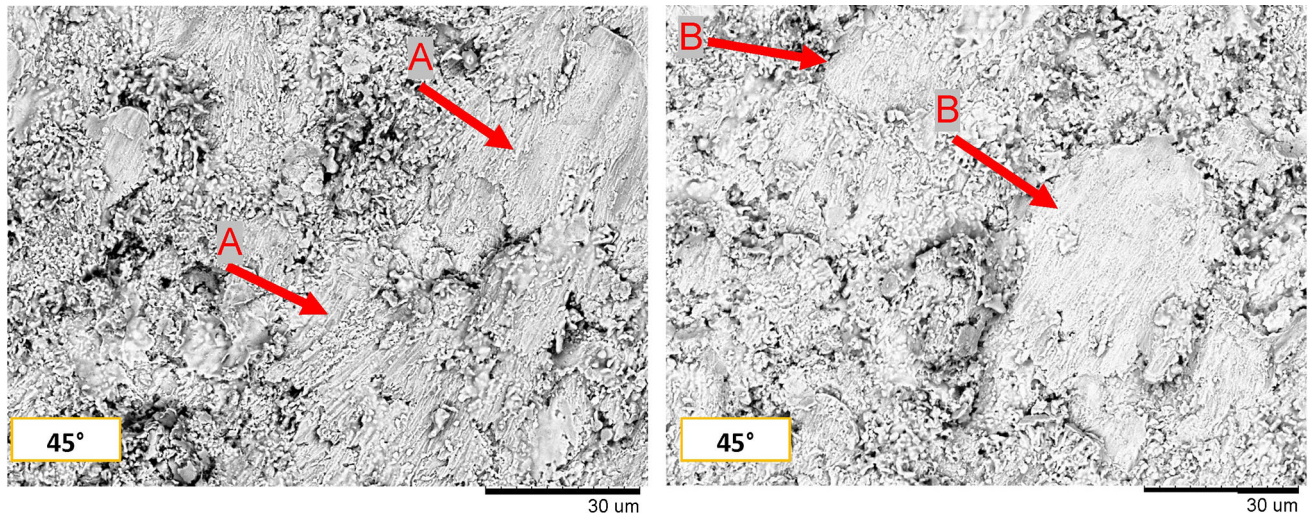
Fig. 4 Both micrographs show the topography of the 45° bond coat. The red arrows marked *A* highlight the smeared surface features. The red arrows marked *B* highlight features that appears to be larger particles that had been sheared off in the coating process (Color figure online)

the material of interest to the mass of the abrasive material (g/g).

Results and Discussion

The following sections describe the results obtained from this study with added discussions and comparisons with past studies.

Bond Coat Deposition and Topography

The target thickness for the bond coat was 200 μm, which was measured using the method described in Sect. 2.4.3 at 214 μm after 9 strokes when sprayed at 90°. At a 45° spray angle, the number of strokes increased to 31 while reaching a thickness of 193 μm.

Figure 3 presents a comparison between the different spray angles for the bond coat topography. The surface roughness of the bond coat produced with 45° spraying was measured at Sa = 3.1 ± 0.5 μm, which was lower than the bond coat produced at 90° of Sa = 6.5 ± 0.5 μm, which is itself comparable to the results shown in the literature by Gupta et al. (Ref 37). As shown in Fig. 3, on the surface of the coating sprayed at 45°, larger semi-deformed particles are not present, which explains the lower Sa value. The coating produced with 45° presented smaller semi-deformed particles in the range of 9-23 μm, manually counted to 2-5 per 1000 μm^2 based on five micrographs taken with SEM. If the deposition rate was similar to a 90° spray

angle, these semi-deformed particles of larger size (>55 μm) would appear more frequently on the surface, as with their appearance in a previous study by Gupta et al. (Ref [37]). The surface also appears to have smeared splat features in a unified direction, which means that the splats are smeared along the surface in the spray direction (Fig. [4]).

The HVAF feedstock with larger particles is expected to form coatings featuring semi-deformed/semi-molten particles on the surface (Ref [37], [38]). Due to the relatively lower thermal input of HVAF, larger particles may not fully melt or not sufficiently soften upon impact. The adhesion of the material on the substrate heavily depends on the particle's kinetic energy just before impact (Ref [21], [39]). The formula for kinetic energy is shown in Eq. [4]:

$$K_E = \frac{1}{2}mv^2 \tag{Eq 4}$$

where m is the particle mass, and v is the particle velocity. As the particle impacts the substrate, its kinetic energy leads to impact energy and thus plastic deformation of the particle. Presumably, it appears that these larger particles will not have enough impact energy to deform and adhere to the substrate and therefore deflect upon impact. This may have to do with the following: (i) Insufficient heating and thus softening of these particles make them more resistant to plastic deformation because more energy is required to heat up larger particles. (ii) Inadequate velocity due to larger particles needing more energy to accelerate and thus not achieving the same speed as the smaller particles. Therefore, the impact energy will be insufficient to mechanically interlock with the substrate/coating upon impact. It is possible that the larger semi-deformed particles partially adhere to the surface, but the majority of the particles are sheared off momentarily after impact. This idea comes from observations on the larger flat smeared features that can be seen on the top surface in Fig. [4]; however, this is difficult to confirm.

Top Coat Deposition and Topography

The top coat spraying process was evaluated through deposition-per-pass (DP). DP is an essential parameter that displays the coating thickness divided by the number of spray passes needed to build up the coating and provides an estimate of the process efficiency (Ref [40]). The coatings on samples T90, T70, T50, and T90B45 showed a similar DP in the interval of 3.1-3.3 μm/pass, while the T30 showed a notable decrease to 1.7 μm/pass.

However, thickness measurements were performed perpendicular to the substrate and did not take the coating density into account; therefore, an evaluation of process
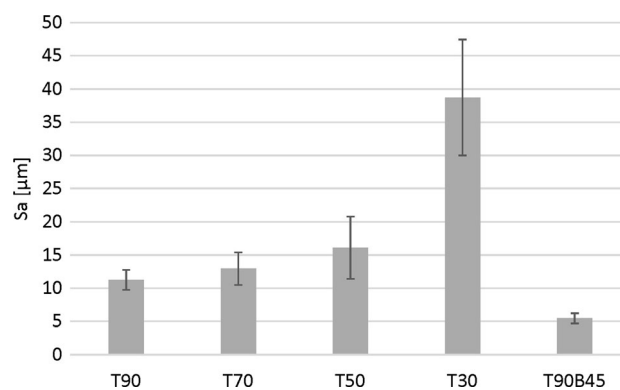
Fig. 5 Area roughness values of the different top coats

efficiency that is based on thickness measurements should be taken with caution.

Figure [5] shows the surface roughness measurements for the top coats, and overview micrographs of the topography can be seen in Fig. [6]. A slight roughness increase was seen along with a decrease in the top coat spray angle in samples T90, T70, and T50, but a more drastic increase was observed when the spray angle was reduced to 30°. With a decrease in spray angle, the topography changed from a cauliflower pattern (T90) to something resembling an artichoke pattern (T30). The cauliflower pattern consisted of each columnar top, but the top of the angular columns was not directly visible when viewed from above, hence the larger artichoke pattern. The surface features grew larger with a decrease in spray angle because more of the columnar stems were visible from above. T90B45 had smaller cauliflower surface features than T90 and appeared to have greater columnar density, which would lead to a smoother top coat surface. The influence of the smoother bond coat surface leads to thinner columns with greater columnar density in the coating. The nanosized YSZ particles build upon the peaks of the coating surface as they follow the impingement jet streamlines parallel to the coating surface. The lower roughness of the T90B45 bond indicates an increase in peak density; the mechanism behind the high density of columns that form on smooth surfaces is explained in detail in Ref [23], [41-43].

Microstructure Analysis

Bond Coat Microstructure

One benefit of synthesizing bond coats using high-velocity thermal spray processes such as HVAF is the dense coating. If the flattening of the droplets or particles is high, then small voids between the lamellar splat structure of the coating will have little to no occurrence. It is known that an off-normal spray angle can cause a higher degree of porosity in the coating due to a phenomenon called
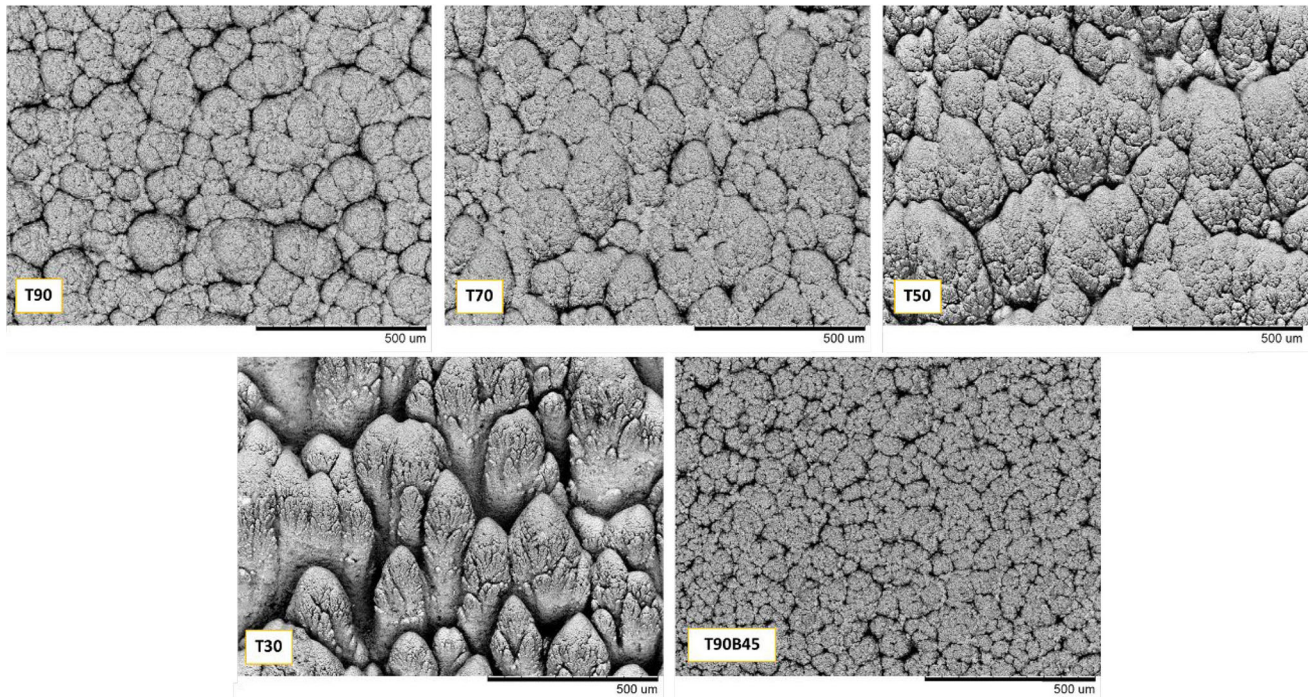
Fig. 6 Topography view for the different top coats
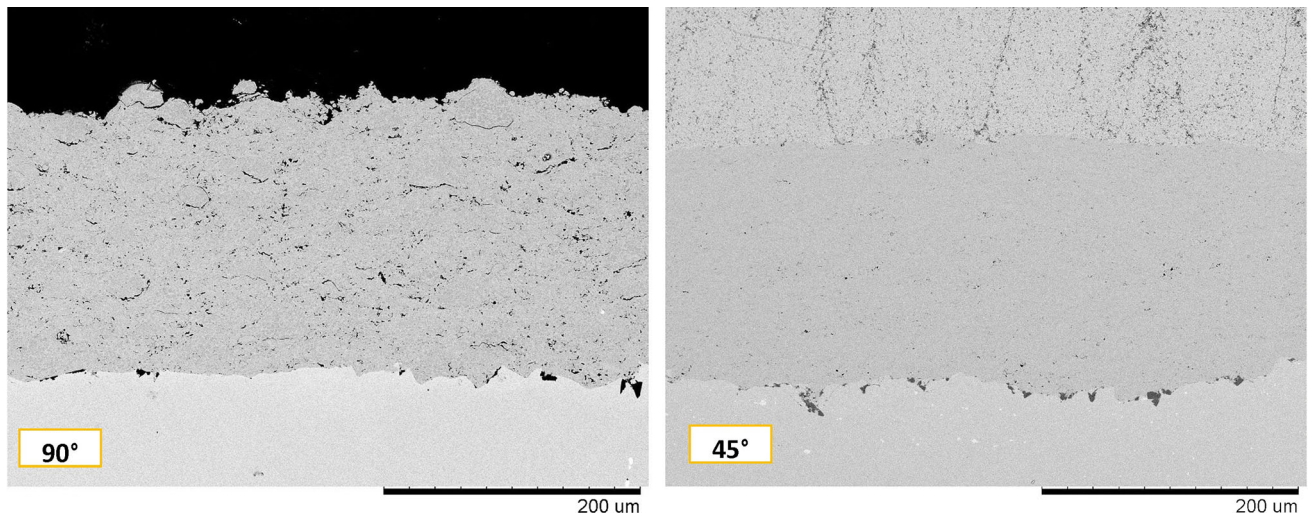
Fig. 7 Microstructure of the bond coats. Left: Amdry 386 sprayed at 90°. Right: Amdry 386 sprayed at 45°

"shadowing" (Ref 39). As droplets hit the surface, the splat formation is uneven in all directions. The droplets may form splats that solidify closer to oval shapes rather than circular when viewed from above (Ref 40). These splats may also have an uneven thickness when viewed from a side profile where the thickness gradually increases in the positive horizontal directional component of the jet stream or impact. The thicker side of the splat may leave a shadowing area, which is a line-of-sight void that subsequent splat formation does not fill up, resulting in a pore.

Porosity formation due to shadowing occurs with APS and other thermal spray methods of similar jet velocities. However, high-velocity thermal spray processes such as HVOF do not form porosities at an off-normal angle (at least not up to 45°) (Ref 39). This is because of the high pressure upon droplet impact. Capillary pressure occurs at the interface between the droplet and the shadowing void (gas) and is significantly greater than the atmospheric pressure. The greater pressure developed by HVOF (and HVAF) would cause the shadowing voids to be filled in by
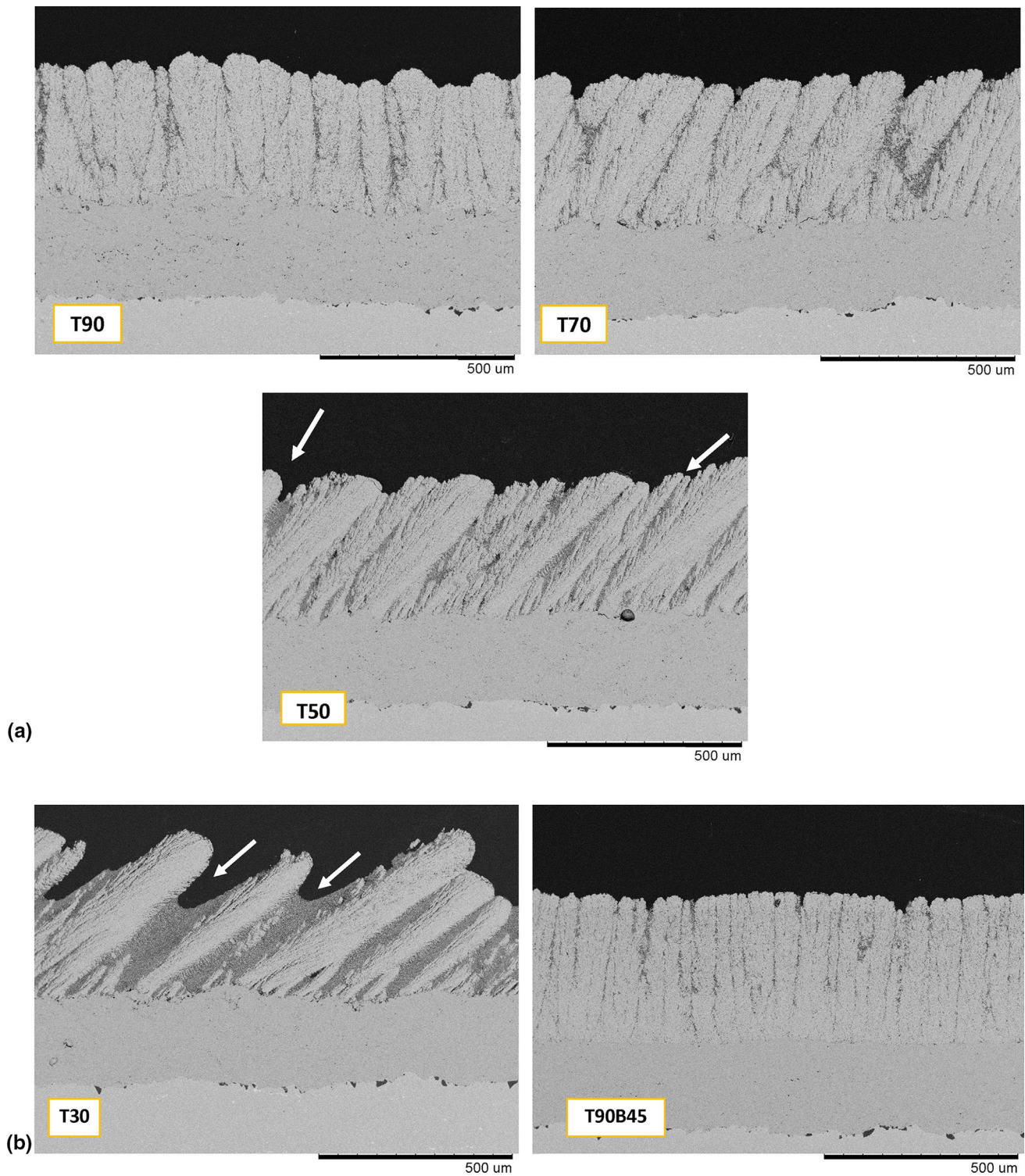
Fig. 8 (a) and (b) Micrographs of cross sections for different spray angles

the subsequently sprayed material. Liquid droplets may not occur during impact using the HVAF system; therefore, sufficient pressure and plastic deformation are needed to form a dense coating at a 45° spray angle, which could be partially achieved with a higher velocity. Furthermore, an off-normal angle may cause a pressure drop where the particle pressure reduces by a factor of cos α, where α is the spray angle. This reduction in pressure may lead to weaker splat bonding and higher levels of porosity (Ref 40, 44).

Comparing the microstructure of the bond coat sprayed at 45° to that sprayed at 90° in Fig. 7, notably fewer interlamellar cracks and pores can be observed in the off-normal sprayed coating. The lack of larger semi-deformed particles led to fewer instances of interlamellar cracks and pores since these particles cause line-of-sight shadow areas and adhere poorly to the substrate/coating. The HVAF system apparently provided sufficient high temperature and velocity to plastically deform the particles upon impact while filling in most shadowing pores that may otherwise occur.

Top Coat Microstructure

The different cross sections in Fig. 8(a) and (b) show the classic SPS microstructure features, such as columns, column gaps, and pores. The columns are tilted at roughly the same angle to the surface plane as the spray angle. This behavior was also observed by Caio and Moreau (Ref 22) and agrees with previous work performed by the authors (Ref 23). Taking a closer look at the off-normal sprayed coatings, we can see that the columns are longer than the standard normal sprayed coating, and the column length for the T30 coating is almost twice the length of the T90.

When decreasing the spray angle, fewer columns are formed, and larger columnar separation zones are present. The columnar separation zones refer to the area between the columns that are not completely gaps but are mostly built up by YSZ particles with a higher degree of porosity, as indicated by the white arrows in Fig. 8. These zones are present on all coatings. However, at greater angles, actual gaps are clearly visible from the coating top to a certain distance below.

The porous regions between columns can be viewed more prominently on the T30 sample. The width of the porous regions on T30 varied significantly, and some regions had the same width as one column. This could be due to the SPS being sensitive to spray distance, and more particles of lower momentum and thermal gradient are potentially presented if their travel path increases. As previously discussed, the off-normal spray angle causes a line-of-sight shadowing area. This area grows larger with the spray angle, and excessive particles that do not directly hit a column may travel in the impinging jet streamlines for a while longer and therefore experience lower velocities while remaining molten/semi-molten before adhering. This results in particles that may not form splats but remain globular in shape, resulting in a significantly more porous microstructure in regions between the YSZ columns.

Figure 9 presents the column density of the different top coats. It was observed that with the increase in off-normal spray angle, the number of columns per unit length decreases with larger column gaps. The column density for
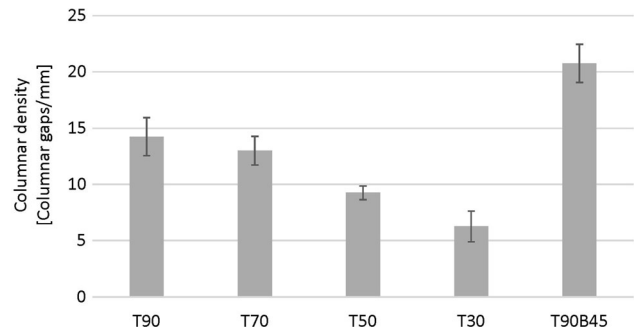

Fig. 9 Overview of the column density

the T90 sample top coat was approximately 14 columns/mm, which was similar to that of a previous study (Ref 36). An increase in the column density was seen on the top coat on sample T90B45, which can be related to the lower surface roughness in the bond coat sprayed at 45°. As discussed previously in Sect. "Top coat deposition and topography", the increased column formation is due to the SPS coating mechanism with the small particles building upon the peaks of the bond coat; these peaks or column initiation points are increased in number with a lower surface roughness (Ref 23, 41-43). The increased column density for sample T90B45 is also shown in Fig. 9, together with an outline of the different spray angles.

Figures 10 and 11 shows micrographs of the microstructure of top coats sprayed with the same parameters on buttons and pistons from a light-duty diesel engine (Region Cc-L and Cx-M) previously studied by the authors (Ref 26). Similar microstructures were identified, but some differences were observed because of the piston shape's influence on the plasma streamlines (Ref 23, 40, 45).

Based on Figure 10(a) and (b), a correlation was observed between the piston microstructure sprayed with a 92° spray angle (Region Cc-L) and that of Sample T90. The link was due to observing a typical SPS microstructure composed of columns, porosity, and column gaps (Ref 42). A difference between the two microstructures was the higher number of columns in the coating sprayed on the piston region, which can be related to the lower roughness of the bond coat in the piston. The higher number of columns can improve the strain tolerance of the coating when it is exposed to temperature variations inside the diesel engine, leading to a higher lifetime for the part (Ref 46).

Figure 11(a) and (b) reveals similarities of the two microstructures sprayed at approximately a 30° spray angle on pistons (Ref 42) and buttons, respectively. The columns presented an inclination of approximately 30° and similar porosity as well as larger column gaps. Marked with white arrows in Fig. 11(a) and (b), the presence of porous regions between the columns was also detected in both coatings.
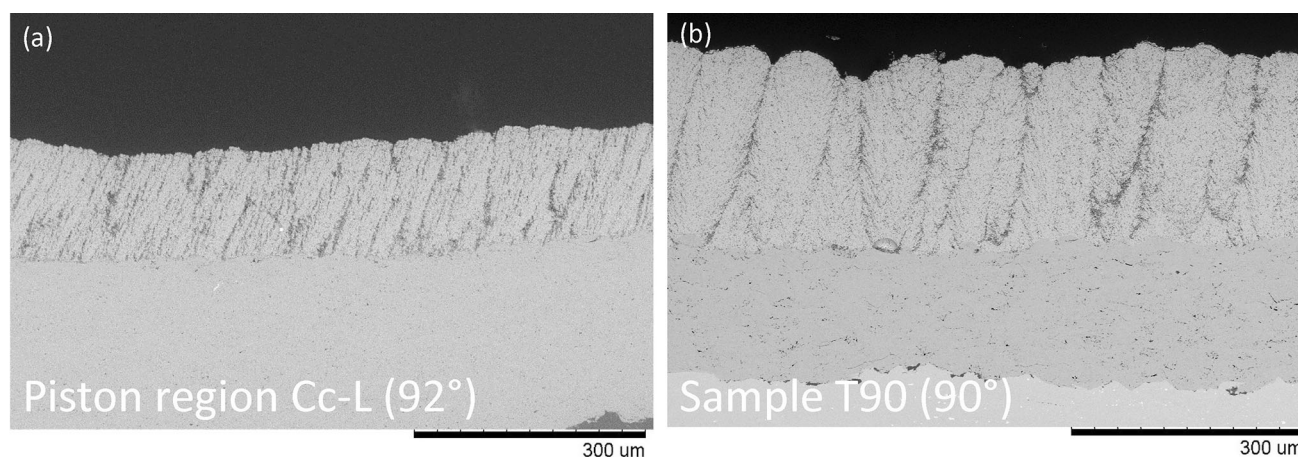
Fig. 10 SEM cross section images of piston region concave with a large spray distance (Cc-L) (a) and sample T90 (b)
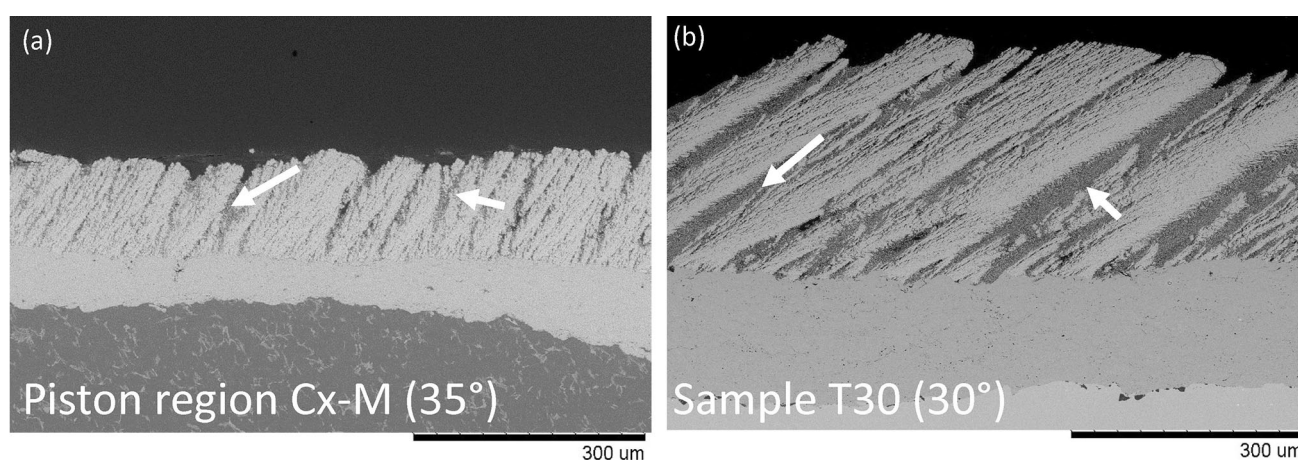
Fig. 11 SEM cross section images of piston region complex with a medium spray distance (Cx-M) (a) and sample T30 (b)

Porosity

The two different groups of porosity, i.e., coarse (>2 μm^2) and fine (≤ 2 μm^2), were measured as described in Sect. "Porosity measurement" using image analysis. The results for the as-sprayed top coats are summarized in Fig. 12, including total porosity as well as coarse and fine porosity. The T30 top coat had the highest total porosity ($\approx 50\%$), followed by T50 ($\approx 45\%$), T70 ($\approx 37\%$), T90B45 ($\approx 31\%$), and T90, which had the lowest porosity ($\approx 29\%$).

A different contribution of each group of porosities was also observed over the different samples. The top coats produced with a 90° spray angle displayed porosity values similar to those found in previous research, which also had a slightly higher contribution from the fine porosity (Ref 10, 11). The off-normal sprayed coatings exhibited a higher degree of coarse porosity with a proportional increase along with the spray angle decrease. This can be related to the microstructural variations shown in Sect. "Top coat deposition and topography" and "Microstructure analysis". The porous zones between the columns are counted as coarse porosity in the image analysis technique, and therefore, coarse porosity becomes noticeably higher with a decrease in spray angle.

Thermal Properties

Figure 13 presents the thermal conductivity (TC) of the coatings based on the thermal diffusivity values and the porosity obtained by image analysis. The study of the thermal properties was limited to coatings T90, T70, T50, and T30, focusing on the variation in the top coat spraying angle. TC was observed to proportionally decrease with increasing porosity, as previously seen (Ref 23, 47-50). This lower TC is associated with the porosity influence due to the lower TC of air inside the pores when compared with bulk YSZ. Porosity can influence the thermal properties in another way, which is the connection between porosity boundaries and phonon scattering. A higher phonon scattering is due to the pore boundaries that increase the travel

**Fig. 12** Porosity of the coatings within the different samples
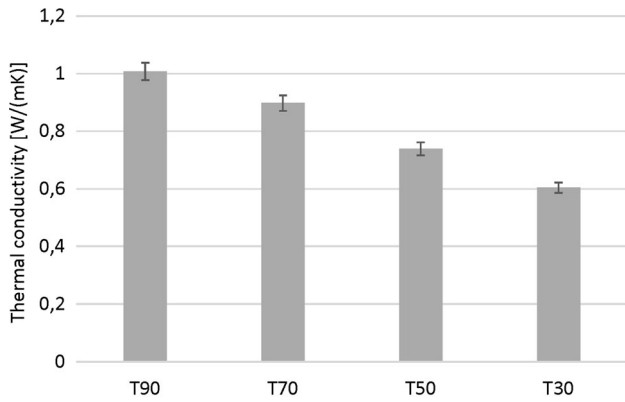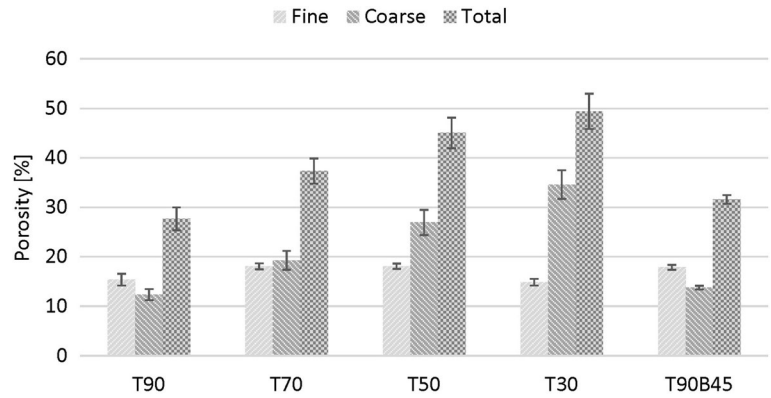
Fig. 13 Thermal conductivity of the coatings within the different spray angles

path and blockage for phonon waves, which can lead to lower thermal conductivity. Similar behavior has been shown in previous studies (Ref 23, 51, 52).

The porous region between the columns influenced the thermal conductivity. The increase in these porous regions with decreasing spray angle lowered the TC. With the increased columnar spacing, more coarse porosity is present in the microstructure. This higher degree of porosity combined with the column inclination leads to changes in the heat flux path within the coating to a higher resistance for the heat flux, and thus, a lower thermal conductivity is found (Ref 47-50, 53). For automotive applications, enhancements in engine efficiency are achieved with coatings with a lower TC, as shown previously (Ref 10, 11). For functional energy application coatings, a low thermal conductivity to shield the component from heat is crucial for operation in hot sections of turbine engines (Ref 54).

Optical Properties

The emissivity results for the coatings produced with different spray angles are presented in Fig. 14 for three different temperatures. The chosen spectral range was
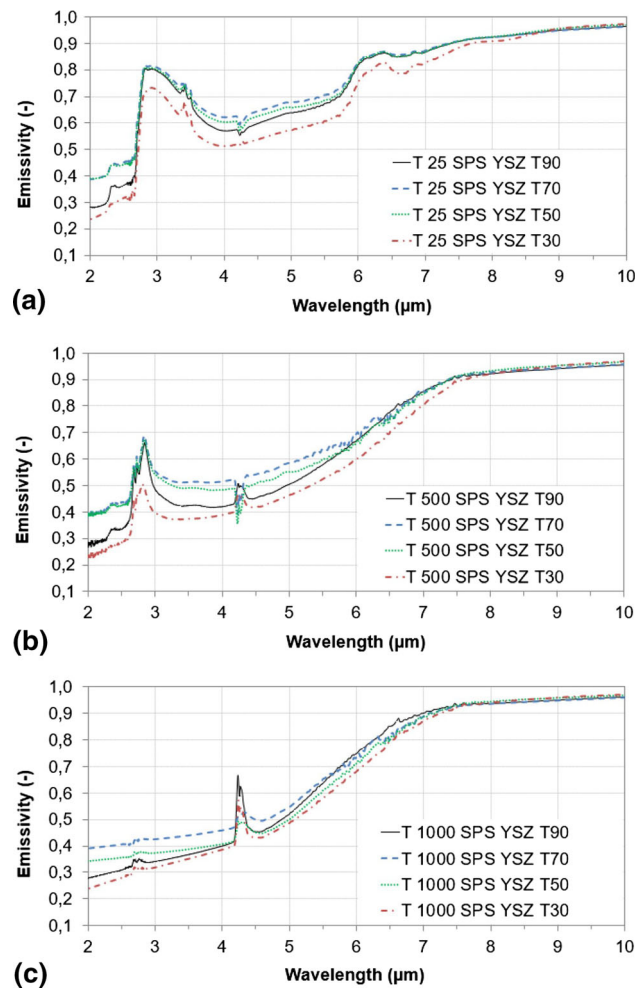

Fig. 14 Emissivity of the coatings sprayed with different spray angles in three different temperatures: A-25 °C, B-500 °C, and C-1000 °C

2-10 μm because it combines the thermal radiation emitted in a turbine engine, i.e., 2-10 μm (Ref 55, 56) with the thermal radiation that is generated in the combustion chamber of a diesel engine, i.e., 2-6 μm (Ref 29, 57). Over the different temperatures in the spectral range from 2 to 7 μm, different emissivities were observed for different

coatings. Above a wavelength of 7 μm, all coatings showed similar emissivity values. For wavelengths of 2-7 μm, there is a marginally lower emissivity observed for the T30 coatings over the different temperatures. Since all samples were polished before the testing of the optical properties, differences in surface roughness can be omitted from the assessment. Based on the lack of difference in roughness, the difference in emissivity can be related to porosity differences. In other words, the higher porosity of T30 led to slightly lower emissivity. Vassen et al. (Ref 58) showed an increase in the reflectivity with higher porosity of APS and SPS YSZ coatings. As shown previously in Sect. "Optical properties" and Eq. 3, the reflectivity is inversely proportional to the emissivity; with this, the results agree with the literature, presenting a high porosity leading to low emissivity coating.

At room temperature, the emissivity uncertainty is less than 3% in the whole spectral range but increases with sample temperature to 6% at 500 °C and 10% at 1000 °C for short wavelengths. For wavelengths above 7 μm, the
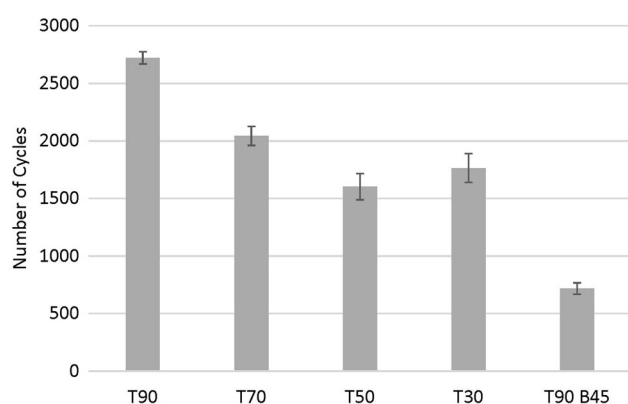
emissivity uncertainty is less than 4%. High values of emissivity uncertainty at short wavelengths are due to the low emissivity of measured materials. The emissivity results are affected by atmospheric absorption in the spectral bands of 2.5-3 μm, 4.2-4.5 μm, and 5-8 μm. Absorption is characterized by peaks and higher emissivity uncertainty (Ref 28, 30).

To maximize the radiation inside a diesel engine or a gas turbine, the TBC should possess a high emissivity in the range of wavelengths at the operating temperature of diesel engines and gas turbines. According to the Planck's law and Wien's displacement law, the maximum radiation intensity is at approximately 3 μm at 700 °C (assumed to be the diesel engine operating temperature), whereas the maximum radiation intensity is at approximately 2.3 μm at 1000 °C (for a gas turbine) (Ref 27).

Coating Testing

In the following sections, the functional property tests performed to evaluate the coatings' capability to work in specific environments for automotive and energy applications are presented.

Flame Rig Test

Figure 15 presents the flame rig test results. It was observed that Sample T90 showed the highest lifetime, which agrees with the authors' previous work (Ref 32). All top coats sprayed with a lower spray angle had a reduced lifetime. This behavior can be associated with the microstructural variations, as discussed in Sect. "Top coat deposition and topography" and "Microstructure analysis", in column inclination and increased porosity. Samples T30 and T50

Fig. 15 Flame rig test results
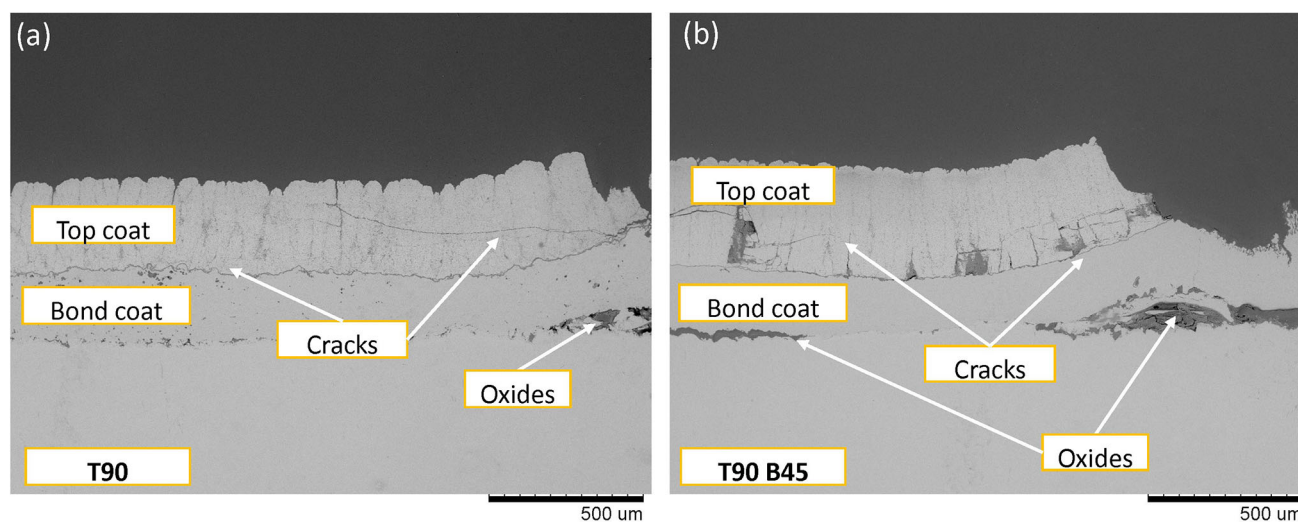
Fig. 16 SEM cross section image after flame rig test of samples T90 (a) and T90B45 (b)
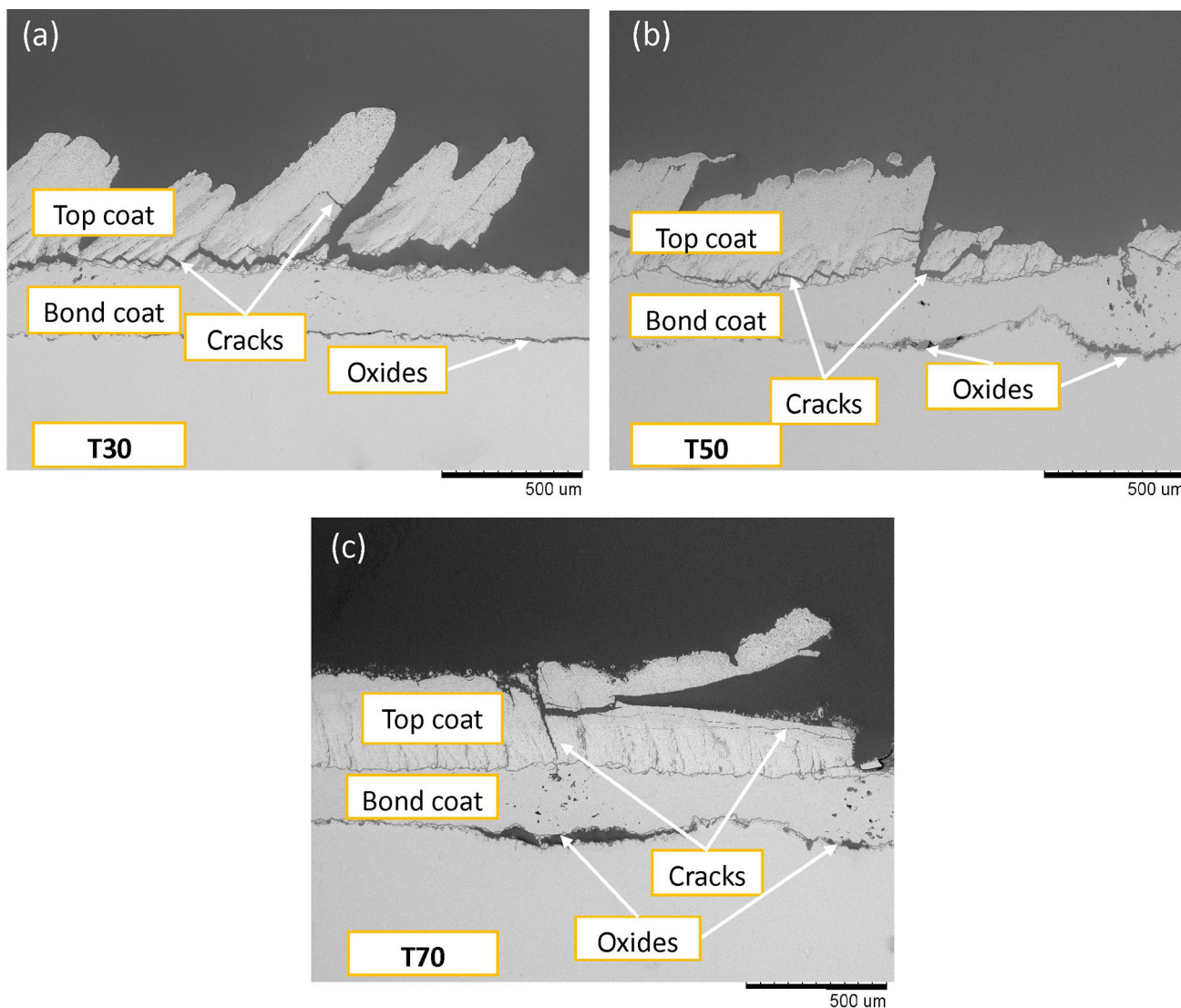
Fig. 17 SEM cross section image after flame rig test of samples T30 (a), T50 (b) and T70 (c)

had an inferior performance with a lower lifetime than the other samples produced with different top coat spray angles. This performance can be related to the extreme column inclination combined with the higher porosity. These differences affected the coating performance because the typical columnar microstructure is altered. With these changes, the major advantage of the SPS coatings to provide high strain tolerance was lowered (Ref 59, 60).
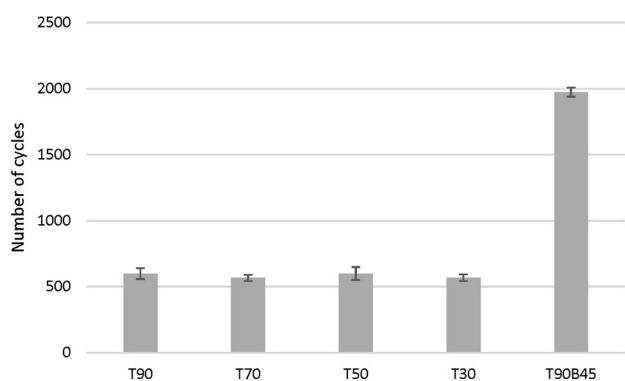
Next, the second-highest lifetime was observed in Sample T70; as shown in Sect. "Microstructure analysis", the microstructural changes (column inclination and increased porosity) are not as extensive as in Samples T30 and T50, which can explain the higher lifetime. The lowest performance within all the sprayed coatings was observed for Sample T90B45. This performance can be related to the microstructural changes due to the influence of the bond

coat roughness on SPS top coating formation. With the lower bond coat roughness and the SPS coating building mechanism explained in Sect. "Top coat deposition and topograph", a high number of columns was observed.

After the flame rig test, the investigated samples were cut on cross section and prepared using the standard preparation procedure for microstructural observation of TBC coatings. The failure was seen as horizontal cracks propagating along the interface between the bond coat and the top coat. In addition to horizontal cracking, the porous area between the column gaps represents a low-energy pathway for crack propagation. The micrographs shown in Fig. 16(a) and (b) are for the T90 and T90B45 microstructures, respectively.

In Fig. 16(a), the presence of oxides at the bond coat/substrate interface on Sample T90 was observed. These oxides might occur because of the exposure of the

substrate to the bond coat and top coat delamination. These oxides can also result from substrate oxidation due to the substrate material being automotive steel. The oxides are generated by the combination of the high heat from the flame (accentuated after top coat delamination) and air from existing pores (internal oxidation) or crack development (after the first oxides grow) through the bond coat. After the formation of oxides, delamination occurs due to the stresses introduced by the oxides combined with the stresses arising from the disparity in thermal expansion between the top coat and the bond coat (Ref 32). In Fig. 16(b), the short lifetime for Sample T90B45 was elucidated by observing a large amount of oxides in the bond coat/substrate interface. These oxides led to higher

stresses within the coatings. These stresses resulted in several cracks along the top coat, and as an outcome, the lifespan of this coating was shortened. The microstructures after the testing for Samples T30, T50, and T70 are shown in Figure 17(a), (b), and (c), respectively.

Figure 17(a) shows that for Sample T30, there is delamination of the top coat with cracks along the top coat/bond coat interface. These cracks can be due to stresses produced by oxides on the bond coat/substrate interface, as shown previously for Samples T90 and T90B45. These oxides, combined with the inclination of the columns and increased porosity of the SPS coating due to the top coat spray angle, lowered this coating's lifespan. Figure 17(b) with Sample T50 and Fig. 17(c) with Sample T70 exhibited the same features, with cracks on the top coat and oxides along with the bond coat/substrate interface. This oxidation can be, as previously correlated, part of the failure mechanism for these coatings, together with the impact of the inclination of the columns and increased porosity on the general high strain tolerance of the SPS coatings.

Thermal Cyclic Fatigue Test

Figure 18 presents the TCF test results for the coatings. Considering the top coat, TCF lifetime does not seem to notably change with an increase in column inclination.
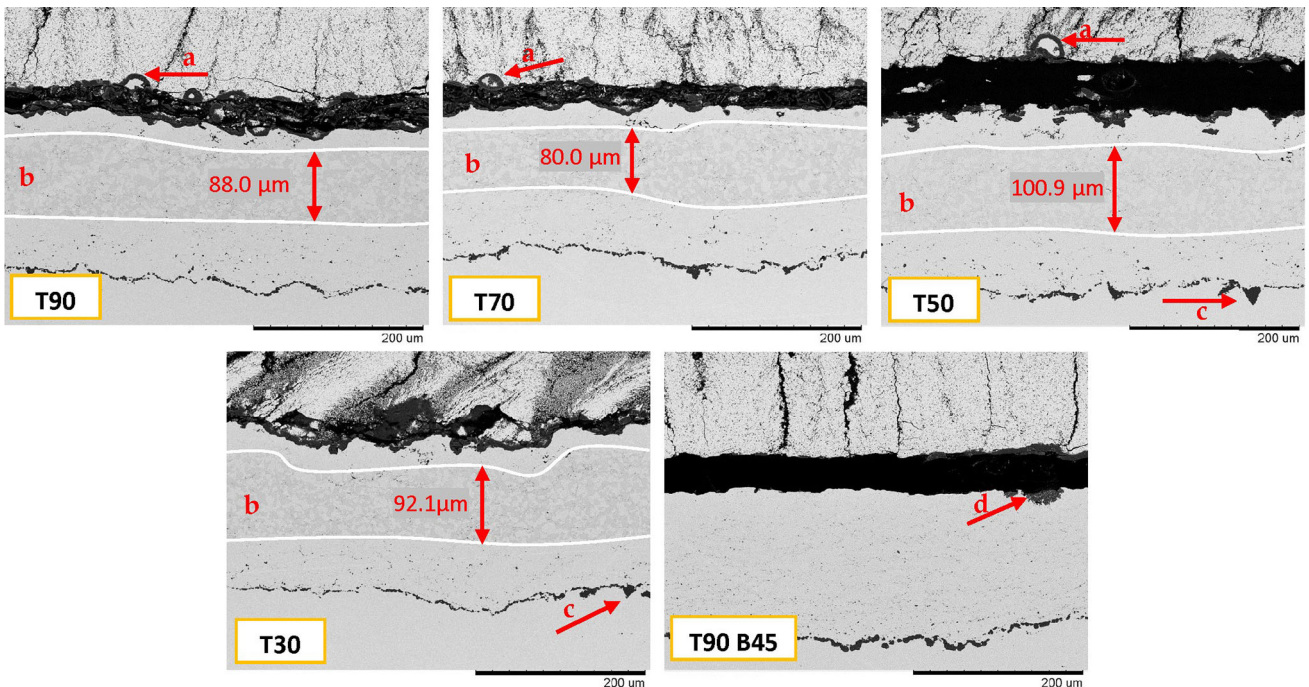

Fig. 18 TCF lifetime of the TBC's
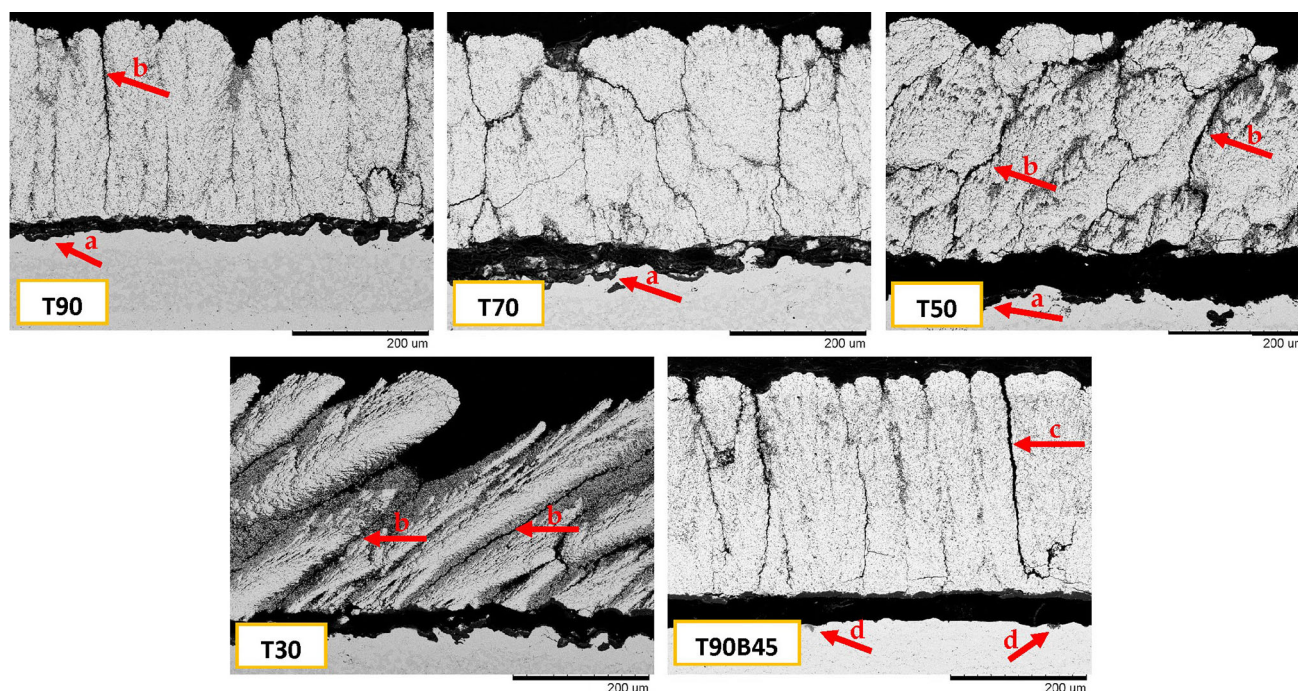
Fig. 19 Cross section images of the coatings after TCF testing; (a) alumina oxide growth. (b) opening of columns. (c) larger column openings on the T90B45 coating. (d) Oxide growth
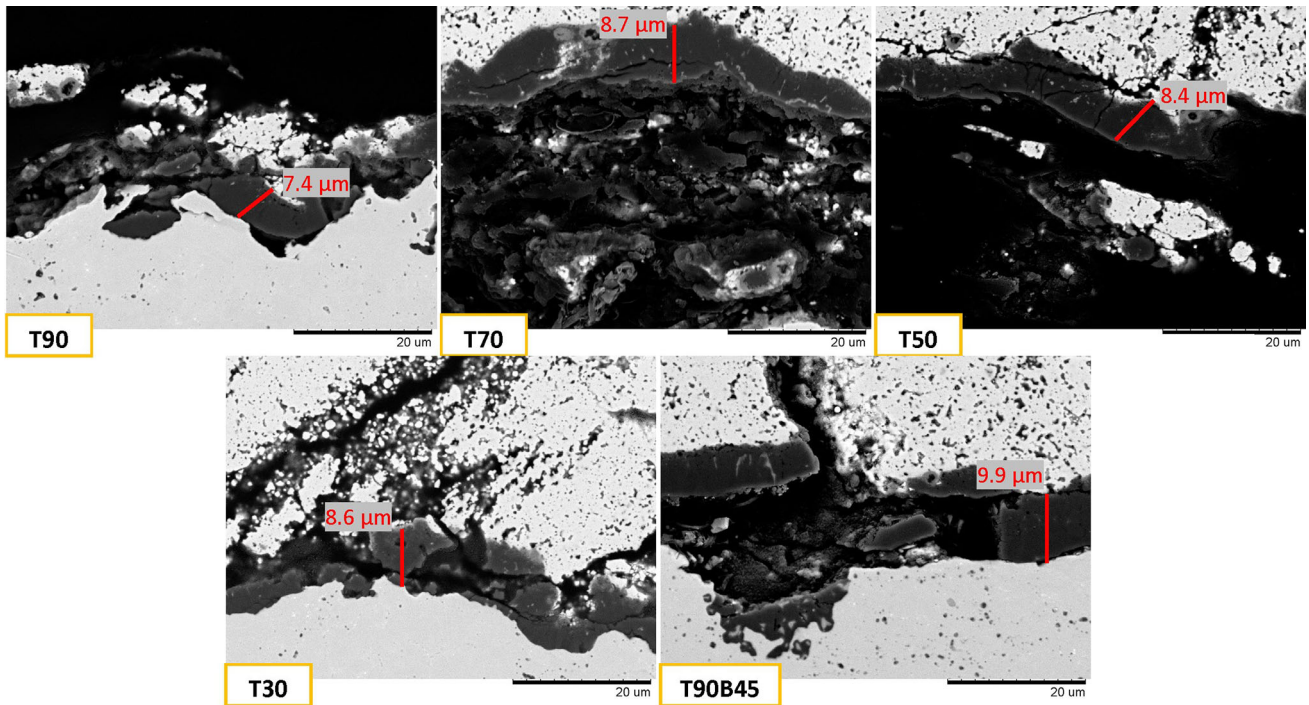
Fig. 20 A closer view of the TGO after the TCF test. Thickness measurements at specific locations are marked in the figure


Fig. 21 The coatings after TCF test where the bond coat and TGO are in focus. (a) semi-deformed particles surrounded by the TGO, separated from the bond coat. (b) The β Ni-Al phase band. (c) Alumina remnants from grit blasting. (d) Oxide growth

However, Sample T90B45 had an almost three times higher lifetime than the other coatings.

Because the samples were uniformly heated and there were relatively long thermal cycles between cooling, the top coat microstructure is believed to have less of an impact in a TCF test than it does in a flame rig test. Micrographs of the failed coatings (Fig. 19) show that the failure was due to excessive thermally grown oxide (TGO) formation, which would impose significant stresses in the bond coat/top coat interface (Ref 69). Thermal mismatches
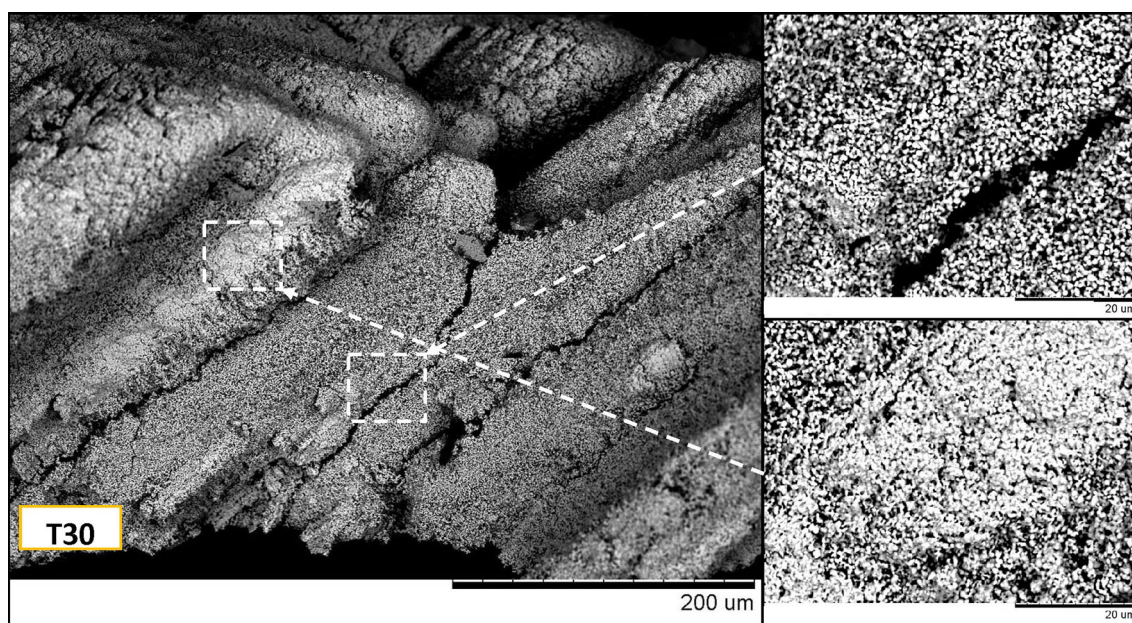
Fig. 22 Cross section view of the T30 coating after the TCF test. The white arrows on the image indicate the vertical cracking with the intercolumnar gaps and a closeup on the porous spherical particle formation compared to the denser splat formation

between the coating layers and TGO contribute to TGO cracking and ultimately coating failure. The micrographs in Fig. 20 show a similar TGO thickness of 8-10 μm in all coatings, where Sample T90B45 only had a slightly thicker TGO at places between 10 and 13 μm. The TGO thickness for the T90 to T30 coatings coincides well with previous studies (Ref 38, 61).

Furthermore, the narrow and straight columns with a tight intercolumn gap seen in Sample T90B45 made the coating structure more compliant with thermal stresses during cyclic heating and forced cooling. Although good for coating anchoring, a rougher bond coat with greater peaks and valleys causes further stresses (e.g., tension in peaks and compression in valleys) in the formed TGO as the samples expand and contract during the thermal cycles. These stresses, in turn, lead to earlier cracking in the TGO, where heat and oxygen in the atmosphere can pass through (Ref 38, 63, 64). The smoother off-normal sprayed bond coat leads to delayed crack formation in the coating because of lesser stresses in TGO and thus a longer TCF lifetime. It is important that Al can diffuse to the bond coat/TGO interface so that it can continuously form/repair the TGO consisting mainly of slow-growing α-alumina that protects the bond coat from other harmful oxide growth (Ref 65, 66). Another possibility behind the longer lifetime of T90B45 is its microstructure. If the number of oxide stringers is larger or their thickness greater then it could further make it difficult for Al to diffuse to the bond coat/TGO interface. By visually comparing the microstructure between the bond coats sprayed at 90° and 45°, it can be
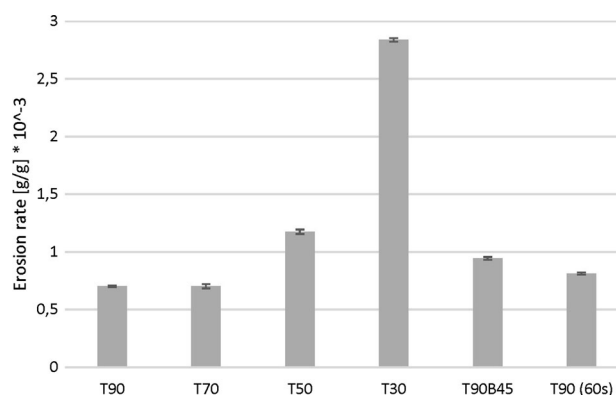

Fig. 23 The erosion rate

seen that the coating sprayed at 45° had significantly thinner oxide stringers and almost no interlamellar cracks.

Furthermore, when analyzing the β Ni-Al phase layer marked with white lines in Figure 21 for the TBCs, similar thicknesses of this layer between the coatings were observed. Since the chemistry was the same and the lifetime was similar, it can be said that an increased spray angle of the top coat does not have a significant impact on the TCF lifetime. However, since the β-phase layer is relatively thick, the coatings had the potential to last longer during the TCF test (Ref 67). As shown in the micrographs presented in Fig. 21, no β Ni-Al phase band could be seen in the T90B45 bond coat, suggesting that the Al reservoir had been depleted. It is believed that a denser bond coat and a more thermally compliant columnar top coat are the main reasons behind the T90B45 long TCF lifetime.
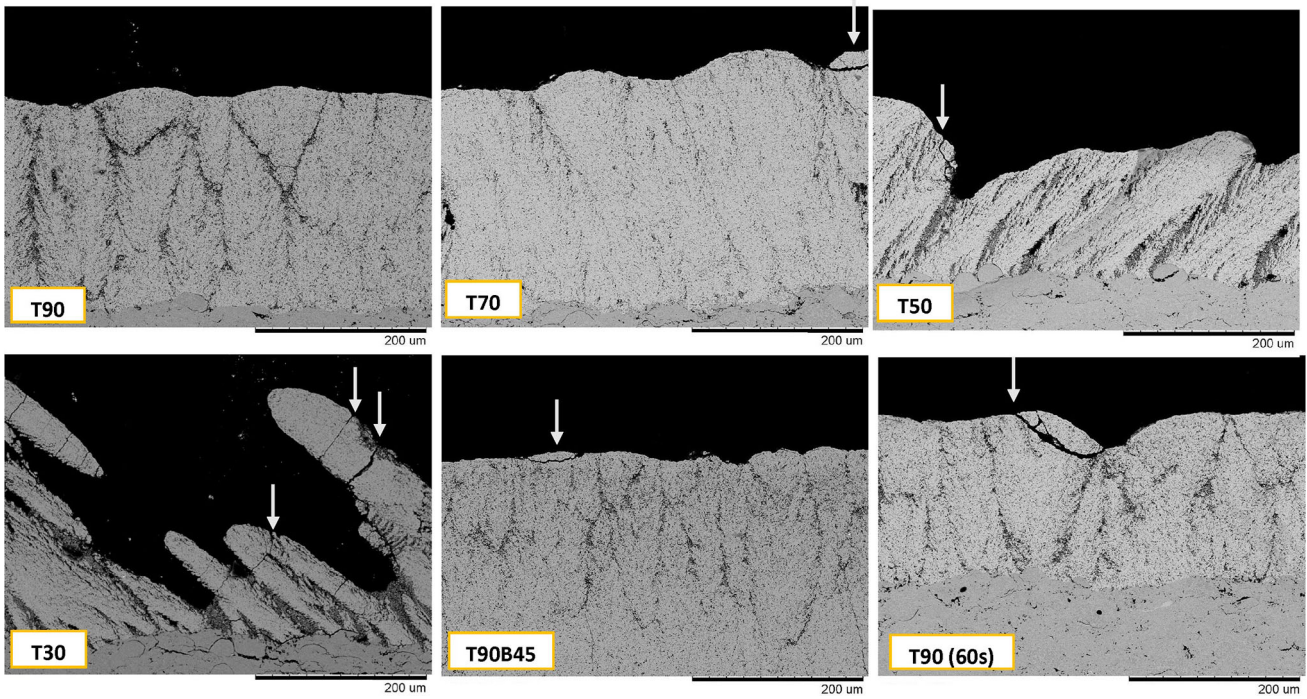
Fig. 24 Cross section image of the tested coatings
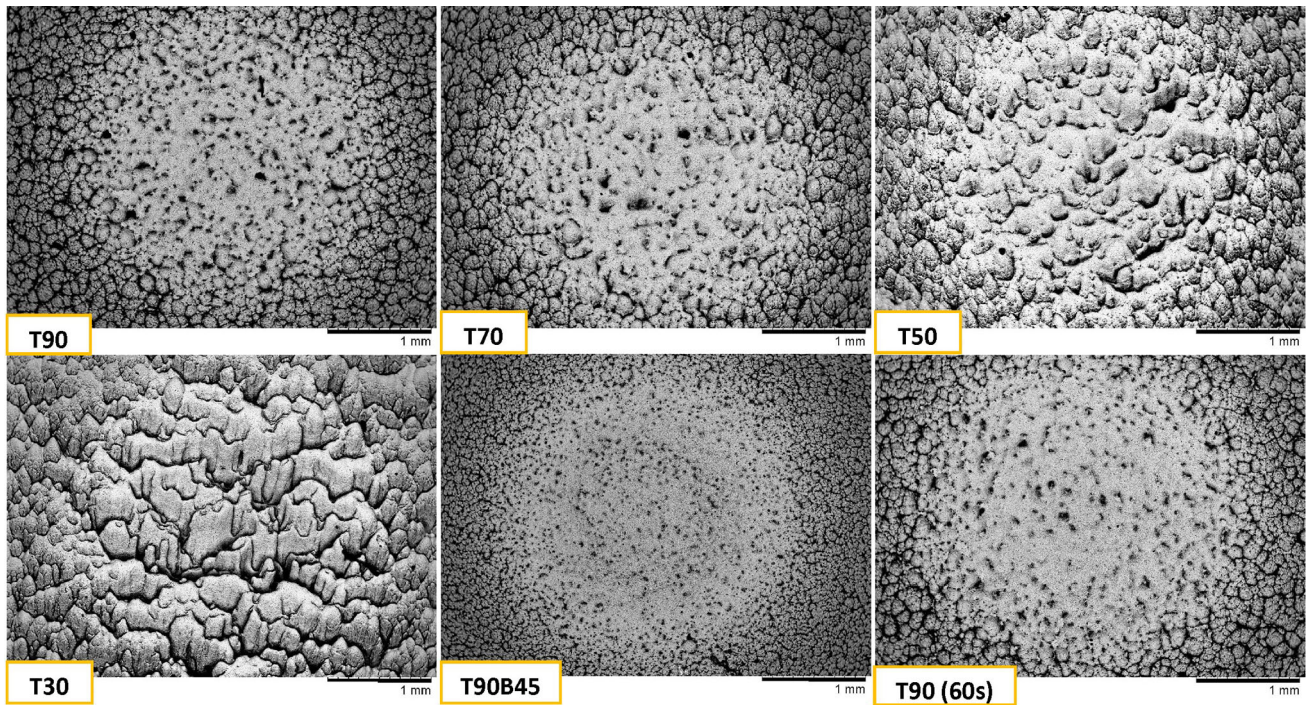
Fig. 25 Overview of the craters after the erosion test

The porous areas between the columns are weak, and cracks can be observed along the columns (Fig. 22), which may be related to the substrate thermal expansion. The porous area between the columns is torn apart as the substrate is uniformly heated and expanded. As the region consists of loosely bonded spherical-shaped particles, it serves as an easy pathway for crack propagation coinciding with a similar observation from a previous study (Ref 63).

Erosion Test

Figure 23 presents the results from the erosion test. Samples T90 and T70 were similar and showed the highest erosive resistance of all the coatings, possibly due to their similar microstructural characteristics, as shown previously in Sect. 3.3. The erosive resistance was lowered with a further decrease in the top coat spray angle. These results are consistent with those of Wellman and Nicholls (Ref 68), which concluded that an inclination of 15° off-normal (90°-75°) would be the maximal angle before the erosion rate becomes substantial.

Previous studies have shown that cracks progress along the weakest points of the microstructure, such as coarse porosity regions, microcracks, and around inclusions (Ref 11, 36, 63). Considering the porosity measurements presented in Fig. 12, a correlation was seen between the porosity and the erosion test results. The coating on Sample T90B45 presented a considerable difference from the other coatings when looking at the relationship between porosity and erosion test results. The coating has similar porosity levels as T90 and T70; however, the coating on Sample T90B45 showed a lower erosion resistance. This lower erosion resistance could be due to the narrower columns that may break off more easily during impact. If the path of the crack from its initiation point is shortened, i.e., if the column diameter is small, then the crack may progress through the cross section of the column and break off a section.

In previous studies (Ref 36, 69, 70), the typical crack paths for brittle, porous YSZ coatings progress laterally and conically near the impact of the erodent. Sections of columns would subsequently break off from top to bottom. In Samples T30 and T50, cracks were seen in the midsection of the column where the erosion particles directly hit the coating, as indicated by the white arrows in Fig. 24. This would break off larger sections during the impact of the erodent, which could explain their higher erosion rates. Lateral cracks or cracks along the cross sections of the columns and conical-shaped cracks can be seen on all coatings (Fig. 24). An overview of the erosion craters can be seen in Fig. 25, where the surface features become larger toward the crater center of T50 and T30 because of the columnar tilt.

The exposure time was set for 60 seconds for a T90 sample to compare with a previous study (Ref 36); therefore, one extra test was performed with this parameter. According to weight measurements, the 60 s sample underwent more than twice the weight reduction, which was slightly more than that of the equivalent 30 s test (2.3 times higher), which meant the erosion rate was higher for the 60 s sample. The difference between erosion rates may be due to a nonlinear erosion rate for the coatings where the upper columnar width is greater than the lower, which means that the erosion rate progressively increases as the columnar structure narrows down to the base.

Conclusions

YSZ-based TBCs under different spray angles were made and investigated to determine the best compromise between the SPS columnar microstructure that would be produced in a substrate of complex geometry and the properties of the coatings. The top coats were manufactured with SPS at 30°, 50°, and 70° spray angles, which were then compared with that produced at a 90° spray angle. Additionally, a metallic MCrAlY bond coat was deposited using HVAF at a 45° spray angle for one batch with a standard 90° top coat.

The different bond coat spray angles revealed a lower surface roughness and discrepancies in the unmolten particles presented in the bond coat topography. The top coat sprayed with a lower spray angle displayed a decreased deposition efficiency, together with a higher surface roughness.

Distinct microstructural features were observed in the top coat sprayed with different angles, such as a higher porosity and angular columns with a lower spray angle. However, the typical SPS microstructure was observed with columns, porosity, and column gaps. Due to the higher porosity combined with the inclination of the columns, the thermal properties showed a decreased thermal conductivity with a decrease in the top coat spray angle, and the optical properties presented a marginal decrease in the emissivity with a decreased top coat spray angle.

Significant impacts on the lifetime were noticed in the different tests with variations in spray angle of below 70° (Sample T70). This was seen due to the higher porosity combined with the column inclination change impacting the usual high strain tolerance of SPS coatings. Mainly, the lower spray angle led to a lower lifetime; the exception was the thermal cyclic fatigue test, where the lower spray angle did not lead to a significant drop in the lifetime.

Based on the results, both HVAF and SPS can be used to spray with an angle between 70° and 90°, which is helpful for complex geometries such as turbine blades employed in energy applications or piston heads used in automotive applications, but the optimal coating was sprayed with a spray angle of 90° top coat and spray of 90° bond coat. This outcome indicates a need for iterations with spraying on complex geometry applications until a spray angle between 70° and 90° is attained; otherwise, the microstructural changes can lead to deterioration in properties and lifetime.

References

1. M. Gross, A Planet with Two Billion Cars, *Curr. Biol.*, 2016, **26**(8), p R307-R310.
2. "Worldwide gas turbine report," Turbomachinery magazine, 2020, https://www.turbomachinerymag.com/worldwide-gas-turbine-report/. Accessed 16 March 2021.
3. S. Slade and C. Palmer, Declines are apparent for the next few years, but a market recovery is in sight, n.d., p 15.
4. D.R. Tree, D.C. Oren, T.M. Yonushonis and P.D. Wiczynski, Experimental Measurements on the Effect of Insulated Pistons on Engine Performance and Heat Transfer, *SAE Int.*, 1996, **105**, p 374-385.
5. R. Kamo, N.S. Mavinahally, L. Kamo, W. Bryzik and E.E. Schwartz, Injection Characteristics That Improve Performance of Ceramic Coated Diesel Engines, *SAE Int.*, 1999 https://doi.org/10.4271/1999-01-0972
6. K.Z. Mendera, Effectiveness of Plasma Sprayed Coatings for Engine Combustion Chamber, *SAE International*, 2000 https://doi.org/10.4271/2000-01-2982
7. T. Hejwowski, Comparative Study of Thermal Barrier Coatings for Internal Combustion Engine, *Vacuum*, 2010, **85**(5), p 610-616.
8. M.B. Beardsley, P.G. Happoldt, K.C. Kelley, E.F. Rejda, and D.F. Socie, "Thermal Barrier Coatings For Low Emission, High Efficiency Diesel Engine Applications," SAE International, (1999)
9. W. Uczak de Goes, J. Somhorst, N. Markocsan, M. Gupta and K. Illkova, Suspension Plasma-Sprayed Thermal Barrier Coatings for Light-Duty Diesel Engines, *J. Therm. Spray Technol.*, 2019, **28**(7), p 1674-1687.
10. J. Somhorst, W. Uczak De Goes, M. Oevermann, and M. Bovo, "Experimental Evaluation of Novel Thermal Barrier Coatings in a Single Cylinder Light Duty Diesel Engine. SAE International, (2019)
11. A. Ganvir, S. Joshi, N. Markocsan and R. Vassen, Tailoring Columnar Microstructure of Axial Suspension Plasma Sprayed TBCs for Superior Thermal Shock Performance, *Mater. Des.*, 2018, **144**, p 192-208.
12. W.A. Sirignano and F. Liu, Performance Increases for Gas-Turbine Engines Through Combustion Inside the Turbine, *J. Propuls. Power*, 1999, **15**(1), p 111-118.
13. A.G. Evans, D.R. Mumm, J.W. Hutchinson, G.H. Meier and F.S. Pettit, Mechanisms Controlling the Durability of Thermal Barrier Coatings, *Prog. Mater. Sci.*, 2001, **46**(5), p 505-553.
14. A. Thibblin, "Thermal Barrier Coatings for Diesel Engines," (Stockholm), KTH Royal Institute of Technology, http://urn.kb.se/resolve?urn=urn:nbn:se:kth:diva-212298. Accessed 17 August 2017.
15. T.W. Clyne and S.C. Gill, Residual Stresses in Thermal Spray Coatings and Their Effect on Interfacial Adhesion: A Review of Recent Work, *J. Therm. Spray Technol.*, 1996, **5**(4), p 401.
16. P. Fauchais, J. Heberlein, and M. Boulos, "Thermal Spray Fundamentals. From Powder to Part," Thermal Spray Fundamentals: From Powder to Part, 2013.
17. C. Lyphout and S. Björklund, Internal Diameter HVAF Spraying for Wear and Corrosion Applications, *J. Therm. Spray Technol.*, 2015, **24**(1), p 235-243.
18. L. Pawlowski, Suspension and Solution Thermal Spray Coatings, *Surf. Coat. Technol.*, 2009, **203**(19), p 2807-2829.
19. J. Fazilleau, C. Delbos, V. Rat, J.F. Coudert, P. Fauchais and B. Pateyron, Phenomena Involved in Suspension Plasma Spraying Part 1: Suspension Injection and Behavior, *Plasma Chem. Plasma Process.*, 2006, **26**(4), p 371-391.
20. J.O. Berghaus, S. Bouaricha, J. Legoux, and C. Moreau, "Injection Conditions and In-Flight Particle States in Suspension Plasma Spraying of Alumina and Zirconia Nano-Ceramics," May, 2005, p 2-4.
21. B. Bernard, A. Quet, L. Bianchi, V. Schick, A. Joulia, A. Malié and B. Rémy, Effect of Suspension Plasma-Sprayed YSZ Columnar Microstructure and Bond Coat Surface Preparation on Thermal Barrier Coating Properties, *J. Therm. Spray Technol.*, 2017, **26**(6), p 1025-1037.
22. F. Caio and C. Moreau, Influence of Substrate Shape and Roughness on Coating Microstructure in Suspension Plasma Spray, *Coatings*, 2019, **9**(11), p 746.
23. W. Uczak de Goes, N. Markocsan and M. Gupta, Microstructural Changes in Suspension Plasma-Sprayed TBCs Deposited on Complex Geometry Substrates, *Coatings*, 2020, **10**(7), p 699.
24. A. Ganvir, N. Markocsan, M.K. Gupta, P. Nylén, C. Moreau, Högskolan Väst, Institutionen för ingenjörsvetenskap, and PTW, "Design of Suspension Plasma Sprayed Thermal Barrier Coatings," (Trollhättan), University West, http://urn.kb.se/resolve?urn=urn:nbn:se:hv:diva-12336. Accessed 16 March 2021.
25. A. Ganvir, N. Curry, S. Björklund, N. Markocsan and P. Nylén, Characterization of Microstructure and Thermal Properties of YSZ Coatings Obtained by Axial Suspension Plasma Spraying (ASPS), *J. Therm. Spray Technol.*, 2015, **24**(7), p 1195-1204.
26. S. Mahade, N. Curry, S. Björklund, N. Markocsan, P. Nylén and R. Vaßen, Functional Performance of Gd2Zr2O7/YSZ Multi-Layered Thermal Barrier Coatings Deposited by Suspension Plasma Spray, *Surf. Coat. Technol.*, 2017, **318**, p 208-216.
27. T.L. Bergman, D.P. DeWitt, F. Incropera and A.S. Lavine, *"Fundamentals of Heat and Mass Transfer*, John Wiley, Hoboken, 2011.
28. P. Honnerová, J. Martan, Z. Veselý and M. Honner, Method for Emissivity Measurement of Semitransparent Coatings at Ambient Temperature, *Sci. Rep*, 2017, **7**(1), p 1386.
29. A. Thibblin, S. Jonsson and U. Olofsson, Influence of Microstructure on Thermal Cycling Lifetime and Thermal Insulation Properties of Yttria-Stabilized Zirconia Thermal Barrier Coatings for Diesel Engine Applications, *Surf. Coat. Technol.*, 2018, **350**, p 1-11.
30. P. Honnerová, J. Martan, M. Kučera, M. Honner and J. Hameury, New Experimental Device for High-Temperature Normal

Spectral Emissivity Measurements of Coatings, *Meas. Sci. Technol*, 2014, **25**(9), p 095501.

31. P. Honnerová, J. Martan and M. Honner, Uncertainty Determination in High-Temperature Spectral Emissivity Measurement Method of Coatings, *Appl. Therm. Eng.*, 2017, **124**, p 261-270.

32. W. Uczak de Goes, N. Markocsan, M. Gupta, R. Vaßen, T. Matsushita and K. Illkova, Thermal Barrier Coatings with Novel Architectures for Diesel Engine Applications, *Surf. Coat. Technol.*, 2020, **396**, 125950.

33. S. Akula Babuprakash and J. Jojo, "Thermophysical and Mechanical Properties of TBC," Jönköping University, (2013).

34. M.K. Gupta, "Design of Thermal Barrier Coatings a Modelling Approach," (Trollhättan), University West, http://urn.kb.se/resolve?urn=urn:nbn:se:hv:diva-7181. Accessed 2 April 2021.

35. ASTM G76-18, 2018 "Test Method for Conducting Erosion Tests by Solid Particle Impingement Using Gas Jets," ASTM International https://doi.org/10.1520/G0076-18.

36. W. Algenaid, A. Ganvir, R.F. Calinas, J. Varghese, K.V. Rajulapati and S. Joshi, Influence of Microstructure on the Erosion Behaviour of Suspension Plasma Sprayed Thermal Barrier Coatings, *Surf. Coat. Technol.*, 2019, **375**, p 86-99.

37. M. Gupta, N. Markocsan, X.-H. Li and B. Kjellman, Development of Bondcoats for High Lifetime Suspension Plasma Sprayed Thermal Barrier Coatings, *Surf. Coat. Technol.*, 2019, **371**, p 366-377.

38. M. Gupta, N. Markocsan, X.-H. Li and R.L. Peng, Improving the Lifetime of Suspension Plasma Sprayed Thermal Barrier Coatings, *Surf. Coat. Technol.*, 2017, **332**, p 550-559.

39. J.R. Davis & Associates and ASM International, Eds., "Handbook of Thermal Spray Technology," (Materials Park, OH), ASM International, (2004)

40. L. Pawlowski, *"The Science and Engineering of Thermal Spray Coatings*, 2nd ed. John Wiley, Hoboken, 2008.

41. N. Curry, Z. Tang, N. Markocsan and P. Nylén, Influence of Bond Coat Surface Roughness on the Structure of Axial Suspension Plasma Spray Thermal Barrier Coatings — Thermal and Lifetime Performance, 6th Rencontres Int, *Proj. Therm.*, 2015, **268**, p 15-23.

42. K. VanEvery, M.J.M. Krane, R.W. Trice, H. Wang, W. Porter, M. Besser, D. Sordelet, J. Ilavsky and J. Almer, Column Formation in Suspension Plasma-Sprayed Coatings and Resultant Thermal Properties, *J. Therm. Spray Technol.*, 2011, **20**(4), p 817-828.

43. P. Sokołowski, S. Kozerski, L. Pawłowski and A. Ambroziak, The Key Process Parameters Influencing Formation of Columnar Microstructure in Suspension Plasma Sprayed Zirconia Coatings, 41st Int, *Conf. Metall. Coat. Thin Films*, 2014, **260**, p 97-106.

44. V.V. Sobolev and J.M. Guilemany, Flattening of Droplets and Formation of Splats in Thermal Spraying: A Review of Recent Work—Part 2, *J. Therm. Spray Technol.*, 1999, **8**(2), p 301-314.

45. T. Ba, C.W. Kang and H.W. Ng, Numerical Study of the Plasma Flow Field and Particle In-Flight Behavior with the Obstruction of a Curved Substrate, *J. Therm. Spray Technol*, 2009, **18**(5), p 858.

46. V. Lughi, V.K. Tolpygo and D.R. Clarke, Microstructural Aspects of the Sintering of Thermal Barrier Coatings, *Mater. Sci. Eng. A*, 2004, **368**(1), p 212-221.

47. A. Ganvir, C. Kumara, M. Gupta and P. Nylen, Thermal Conductivity in Suspension Sprayed Thermal Barrier Coatings: Modeling and Experiments, *J. Therm. Spray Technol.*, 2017, **26**(1), p 71-82.

48. H. Kaßner, A. Stuke, M. Rödig, R. Vaßen and D. Stöver, Influence of Porosity on Thermal Conductivity and Sintering in Suspension Plasma Sprayed Thermal Barrier Coatings, *Ceram. Eng. Sci. Proc.*, 2009, **29**, p 147-158.

49. J. Ekberg, A. Ganvir, U. Klement, S. Creci and L. Nordstierna, The Influence of Heat Treatments on the Porosity of Suspension Plasma-Sprayed Yttria-Stabilized Zirconia Coatings, *J. Therm. Spray Technol.*, 2018, **27**(3), p 391-401.

50. A. Ganvir, N. Markocsan and S.V. Joshi, Influence of Isothermal Heat Treatment on Porosity and Crystallite Size in Axial Suspension Plasma Sprayed Thermal Barrier Coatings for Gas Turbine Applications, *Coatings*, 2016, **7**(1), p 4.

51. A. Kulkarni, A. Vaidya, A. Goland, S. Sampath and H. Herman, Processing Effects on Porosity-Property Correlations in Plasma Sprayed Yttria-Stabilized Zirconia Coatings, *Mater. Sci. Eng. A*, 2003, **359**(1), p 100-111.

52. N. Curry, M. Leitner and K. Körner, High-Porosity Thermal Barrier Coatings from High-Power Plasma Spray Equipment—Processing Performance and Economics, *Coatings*, 2020, **10**(10), p 957.

53. I.O. Golosnoy, A. Cipitria and T.W. Clyne, Heat Transfer Through Plasma-Sprayed Thermal Barrier Coatings in Gas Turbines: A Review of Recent Work, *J. Therm. Spray Technol.*, 2009, **18**(5), p 809-821.

54. S. Bose and J. DeMasi-Marcin, Thermal Barrier Coating Experience in Gas Turbine Engines at Pratt & Whitney, *J. Therm. Spray Technol.*, 1997, **6**(1), p 99-104.

55. R.A. Rooth and W. Hiemstra, Dual Wavelength Temperature Monitoring of TBC Coated Alstom 13E2 Turbine Blades, *ASME Turbo Expo*, 2003, **2003**, p 581-588. https://doi.org/10.1115/GT2003-38814

56. J. Tian, T. Fu, Q. Xu and H. Jiang, Effective Spectral Emissivity of Gas Turbine Blades for Optical Pyrometry, *J. Heat Transf*, 2017, **139**(7), p 072701. https://doi.org/10.1115/1.4035732

57. V. Merzlikin, V. Timonin, M.G. Ojeda and O. Sidorov, New Selectively Absorbing and Scattering Heat-Insulating Coatings of the Combustion Chamber for Low-Heat-Rejection Diesel, *SAE World Congress Exhibition*, 2007 https://doi.org/10.4271/2007-01-1755

58. R. Vaßen, H. Kassner, A. Stuke, D.E. Mack, M.O.D. Jarligo, and D. Stöver, Functionally Graded Thermal Barrier Coatings with Improved Reflectivity and High-Temperature Capability, Mater. Sci. Forum, Trans Tech Publications Ltd, (2010), 631-632, p 73–78.

59. P. Sokołowski, L. Pawłowski, D. Dietrich, T. Lampke and D. Jech, Advanced Microscopic Study of Suspension Plasma-Sprayed Zirconia Coatings with Different Microstructures, *J. Therm. Spray Technol.*, 2016, **25**(1), p 94-104.

60. N. Curry, K. VanEvery, T. Snyder and N. Markocsan, Thermal Conductivity Analysis and Lifetime Testing of Suspension Plasma-Sprayed Thermal Barrier Coatings, *Coatings*, 2014, **4**(3), p 630-650.

61. M. Gupta, N. Markocsan, X.-H. Li and L. Östergren, Influence of Bondcoat Spray Process on Lifetime of Suspension Plasma-Sprayed Thermal Barrier Coatings, *J. Therm. Spray Technol.*, 2018, **27**(1-2), p 84-97.

62. D.R. Clarke, M. Oechsner and N.P. Padture, Thermal-Barrier Coatings for More Efficient Gas-Turbine Engines, *MRS Bull.*, 2012, **37**(10), p 891-898.

63. A. Ganvir, V. Vaidhyanathan, N. Markocsan, M. Gupta, Z. Pala and F. Lukac, Failure Analysis of Thermally Cycled Columnar Thermal Barrier Coatings Produced by High-Velocity-Air Fuel and Axial-Suspension-Plasma Spraying: A Design Perspective, *Ceram. Int.*, 2018, **44**(3), p 3161-3172.

64. D.R. Clarke and W. Pompe, Critical Radius for Interface Separation of a Compressively Stressed Film from a Rough Surface, *Acta Mater.*, 1999, **47**(6), p 1749-1756.

65. E. Sadeghimeresht, N. Markocsan, M. Huhtakangas and S. Joshi, Isothermal Oxidation of HVAF-Sprayed Ni-Based Chromia, Alumina and Mixed-Oxide Scale Forming Coatings in Ambient Air, *Surf. Coat. Technol.*, 2017, **316**, p 10-21.

66. T. Hussain, T. Dudziak, N.J. Simms and J.R. Nicholls, Fireside Corrosion Behavior of HVOF and Plasma-Sprayed Coatings in Advanced Coal/Biomass Co-Fired Power Plants, *J. Therm. Spray Technol.*, 2013, **22**(5), p 797-807.

67. O. Aranke, M. Gupta, N. Markocsan, X.-H. Li and B. Kjellman, Microstructural Evolution and Sintering of Suspension Plasma-Sprayed Columnar Thermal Barrier Coatings, *J. Therm. Spray Technol.*, 2019, **28**(1–2), p 198-211.

68. R.G. Wellman and J.R. Nicholls, A Review of the Erosion of Thermal Barrier Coatings, *J. Phys. Appl. Phys.*, 2007, **40**(16), p R293-R305.

69. C.S. Ramachandran, V. Balasubramanian and P.V. Ananthapad-manabhan, Erosion of Atmospheric Plasma Sprayed Rare Earth Oxide Coatings under Air Suspended Corundum Particles, *Ceram. Int.*, 2013, **39**(1), p 649-672.

70. X. Chen, M.Y. He, I. Spitsberg, N.A. Fleck, J.W. Hutchinson and A.G. Evans, Mechanisms Governing the High Temperature Erosion of Thermal Barrier Coatings, *Wear*, 2004, **256**(7–8), p 735-746.